Journal of Medicinal Chemistry

Article

Bisphosphonate inhibitors of mammalian glycolytic aldolase

Paul Heron, Marta Abellán-Flos, Laurent Salmon, and Jurgen Sygusch

J. Med. Chem., **Just Accepted Manuscript** • DOI: 10.1021/acs.jmedchem.8b01000 • Publication Date (Web): 12 Nov 2018

ACS Publications

is published by the American Chemical Society. 1155 Sixteenth Street N.W., Washington, DC 20036

Bisphosphonate inhibitors of mammalian glycolytic aldolase

Paul W. Heron[§], Marta Abellán-Flos[†], Laurent Salmon[†], Jurgen Sygusch*[§]

*§ Département de biochimie et médecine moléculaire, Université de Montréal. CP 6128, Succursale Centre-Ville, Montréal, Québec, Canada H3C 3J7

† Equipe de Chimie Bioorganique et Bioinorganique, Institut de Chimie Moléculaire et des Matériaux d'Orsay (ICMMO), Univ Paris-Saclay, Univ Paris-Sud, CNRS UMR8182, LabEx LERMIT, rue du doyen Georges Poitou, F-91405 Orsay, France

ABSTRACT

The glycolytic enzyme aldolase is an emerging drug target in diseases such as cancer and protozoan infections which are dependent on a hyperglycolytic phenotype to synthesize ATP and metabolic precursors for biomass production. To date, structural information for the enzyme in complex with phosphate-derived inhibitors has been lacking. Thus, we determined the crystal structure of mammalian aldolase in complex with naphthalene 2,6-bisphosphate (**1**) that served as a template for the design of bisphosphonate-based inhibitors, namely 2-phosphate-naphthalene 6-bisphosphonate (**2**), 2-naphthol 6-bisphosphonate (**3**), and 1-phosphate-benzene 4-bisphosphonate (**4**). All inhibitors targeted the active site and the most promising lead, **2**, exhibited slow-binding inhibition with an overall inhibition constant of ~38 nM. Compound **2** inhibited proliferation of HeLa cancer cells while HEK293 cells expressing a normal phenotype were not inhibited. The crystal structures delineated the essential features of high-affinity phosphate-derived inhibitors and provide a template for the development of inhibitors with prophylaxis potential.

INTRODUCTION

Glucose metabolism in cancer cells is characterized by a marked increase in both glucose uptake and aerobic glycolysis, the fermentation of glucose into lactate in the presence of oxygen. Enhanced glucose uptake in cancer cells is now exploited clinically for diagnostic purposes with positron emission tomography (PET) where radiolabeled glucose (^{18}fluoro-deoxyglucose) is used as a tracer to assay for accumulation in tumors.[1] The latter effect of increased fermentation has been known for several decades, and was first proposed by German physiologist and Nobel laureate, Otto Warburg, who, in the 1920s showed that tumor cells produce higher levels of lactate compared to normal tissues, even in the presence of oxygen.[2] Hyperglycolysis not only produces ATP at a faster rate than oxidative phosphorylation, but also provides metabolic precursors for biomass production (e.g. nucleotide, amino acid, and lipid biosynthesis), aiding in the rapid proliferation of cancer cells.[3] The term "Warburg effect" was coined and ongoing conceptual and empirical advances over several decades have led to the acceptance of altered metabolism as one the hallmarks of cancer.[4] Tumor glycolysis is actively studied as a potential target for cancer therapy, however viable clinical leads have proven elusive.[5]

A leading candidate is fructose-1,6-bisphosphate (FBP) aldolase (EC 4.1.2.13), a central enzyme in glycolysis responsible for the reversible aldol reaction of fructose-1,6-bisphosphate to glyceraldehyde-3-phosphate and dihydroxyacetone phosphate. Glycolytic aldolase is a Class I enzyme, found in eukaryotes and higher plants, and characterized by the formation of a protonated imine (Schiff base) with an active site lysine. Aldolase expression levels were pronounced when investigated in several malignant cell lines such as human lung squamous carcinomas,[6–8] hepatocellular carcinomas,[9,10] pancreatic[11] and colorectal cancers.[12] Aldolase is already a target in parasitic organisms such as *Trypanosoma brucei* (causative agent for African sleeping sickness)

for which glycolysis is the sole source of ATP production.[13,14] Earlier work in the literature and from our laboratory has focused on the development of class I aldolase inhibitors in such organisms.[14,15]

Among these, phosphorylated substrate analogues of fructose-1,6-bisphosphate aldolases possessing an aromatic moiety were of considerable interest due to their ability to strongly interact with the active site. First intended for their interest in probing the nature of the active site, which was assumed to be hydrophobic based on residues surrounding the reactive lysine,[16] these aromatic derivatives were among the most powerful competitive inhibitors of the rabbit muscle aldolase-catalyzed reaction. Notably, these aromatic time-dependent reversible inhibitors (slow-binding) capable of targeting active site lysine residues, namely 2-hydroxybenzaldehyde-4-phosphate[17] and 1-hydroxy-2-napthaldehyde-6-phosphate,[18] inactivated aldolase and implicated a slow reversible Schiff base mechanism. A naphthalenic derivative, naphthalene 2,6-bisphosphate (NA-P_2) was shown to be a potent competitive inhibitor with K_i = 0.28 μM.[18] The mode of inhibition by which these phosphorylated aromatic derivatives inhibited aldolase was established by enzyme kinetics, UV/visible difference spectroscopy and site-directed mutagenesis,[17] yet these studies did not provide detailed structural insight, with the exception of computational modeling studies involving 1-hydroxy-2-napthaldehyde-6-phosphate.[18]

Different types of bis-phosphonate derivatives were previously reported to act as highly effective enzyme inhibitors. In the case of zinc-metallo enzymes such as matrix metalloproteinases and carbonic anhydrase, arylamino-bisphosphonates were used as chelating agents of the active site zinc cofactor, as well as mimics of the tetrahedral high-energy intermediate involved in the catalyzed reaction.[19] Other bisphosphonates derivatives were also reported as potent inhibitors of the Mg^{2+}-dependent farnesyl pyrophosphate synthase[20–22] and geranylgeranyl pyrophosphate

synthase,[20,23,24] acting both as metal binding agents and pyrophosphate mimics. In addition, methylene bisphosphonate inhibitors were successfully employed as inhibitors of HIV reverse transcriptase phosphorolytic activity.[25]

We sought to elucidate the interaction between several phosphorylated aromatic derivatives and the aldolase active site to serve as a template for designing potent high-affinity phosphorylated inhibitors. Here, using the previously known competitive inhibitor NA-P_2 (**1**) as template, we describe the binding of aromatic bisphosphonate substrate analogues of aldolase, namely 2-phosphate-naphthalene 6-bisphosphonate (PNAB) (**2**), 2-naphthol 6-bisphosphonate (NAB) (**3**), and 1-phosphate-benzene 4-bisphosphonate (PBB) (**4**) (Chart 1). The mode of binding was determined by a combination of x-ray crystallography and enzyme inhibition kinetics. The high-resolution crystal structures of these phosphorylated aromatic inhibitors in complex with aldolase are described and should serve as a basis for the design of potent lead compounds.

Chart 1. Bisphosphonate Aromatic Analogues Based on FBP Aldolase Inhibitor **1**[a]

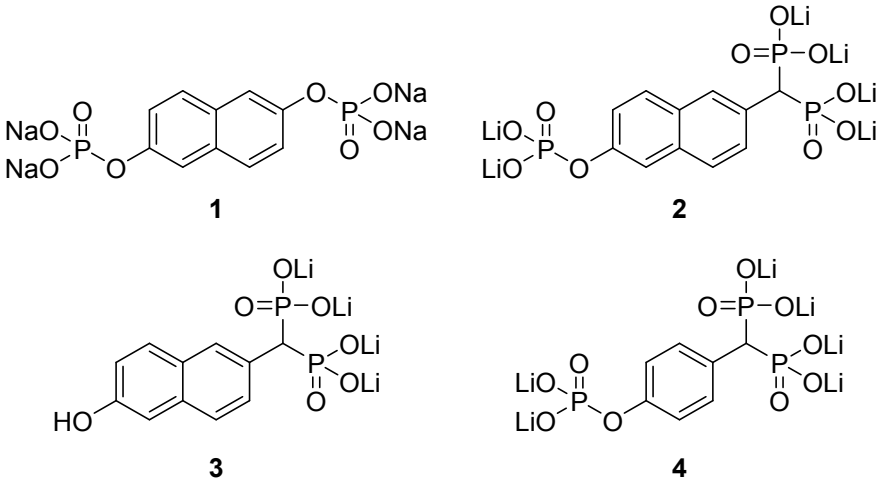

[a] Fructose-1,6-bisphosphate (FBP) aldolase inhibitors: naphthalene 2,6-bisphosphate (**1**, sodium salt, NA-P2),[16,18] 2-phosphate-naphthalene 6-bisphosphonate (**2**, lithium salt, PNAB), 2-naphthol

6-bisphosphonate (**3**, lithium salt, NAB), and 1-phosphate-benzene 4-bisphosphonate (**4**, lithium salt, PBB).

RESULTS AND DISCUSSION

Structure of ALDOA-1 (NA-P_2) complex. To investigate the binding mode of phosphorylated aromatic compounds, rabbit muscle aldolase (ALDOA) crystals were soaked in crystallization buffer containing compound **1**. The rabbit isoform is routinely used for its ease of purification, crystallization, and is a good model candidate for the human isoform because of its exceptionally high homology (98% sequence identity; 100% sequence homology).[26] The final crystal structure was determined to 1.97 Å resolution (R_{work} = 12.87%; R_{free}= 16.65%) and shows a tetramer in the asymmetric unit of space group $P2_1$, consistent with aldolase structures previously reported for these crystallization conditions[27] (see Experimental Section for details). Data collection and refinement statistics for all crystal structures are shown in Table 4 in the Experimental Section. A tetramer in the asymmetric unit cell gives the opportunity to make four independent observations, and, expected from previous work, that the compound should bind in a 1:1 ratio of [inhibitor: subunit].[16]

The overall topology of the active site shown in Figure 1A highlights the basic electrostatic potential surface of the catalytic pocket nestled inside a TIM-barrel. The electron density surrounding the bound inhibitor (Figure 1B) was unambiguous and allowed for confident modeling into the active site of each tetramer subunit. The phosphate binding loci of **1** are homologous with the P_1- and P_6-phosphate binding site of the substrate FBP (shown in Figure S1). A feature of the FBP P_6-binding site was the electrostatic interaction implicating Lys107, described in high-resolution structures[27] and deduced from differential protection experiments.[28] Attachment by **1** involves the same electrostatic interaction with Lys107 at the P_6-site as was found for the substrate, and is consistent with the finding that a Lys107 variant (K107M) exhibits a reduced affinity (higher K_i) for **1**.[18]

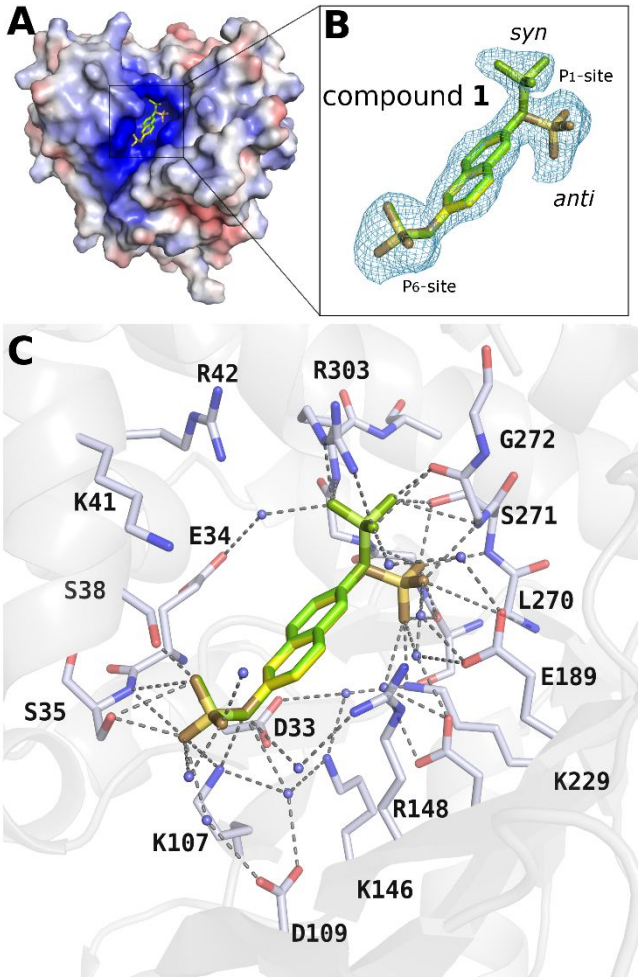

Figure 1. Crystal structure of the ALDOA-**1** complex showing *syn* and *anti* conformers of compound **1**. (A) Electrostatic surface potentials of rabbit muscle aldolase (ALDOA) calculated using the Adaptive Poisson-Boltzmann Solver (APBS) software package with contour field of ± 5 kT/e.[12] Acidic residues are colored *red*, basic residues are colored *blue*. (B) Difference electron density calculated from a 1.97 Å simulated annealing F_o - F_c omit map encompassing compound **1** and contoured at 3.0σ. *Syn* and *anti*- conformations of **1** are shown. (C) Hydrogen-bonding network of **1** with active site residues and water molecules. Notable interactions are those formed by compound **1** phosphate moieties in the P_1- and P_6- phosphate loci of FBP (P_1: vicinal to Arg303; P_6: vicinal to Ser35).

The hydrogen-bonding network of this binding locus is similar to that observed in the Schiff

base complex formed with FBP [PDB id: 1ZAI].[27] Notably, Lys107 interacts with two phosphate oxyanions (contacts of 3.1 Å and 2.9 Å) of **1** and, similarly to FBP, Ser35 and Ser38 hydroxyl groups contact the phosphate oxygens. However, the phosphate moiety of **1** is displaced with respect to the FBP P_6-phosphate by 1 Å beyond the center of the active site cleft, consistent with the longer intramolecular distance between phosphate moieties of 9.8 Å in **1** compared to 8.9 Å in FBP. The flanking helical region (residues 34-65) undergoes a displacement upon binding by **1**, that is smaller by ~1 Å compared to FBP binding and fixes the bound phosphate at the P_6-site (Figure S1). Displacement by this flanking helix has been noted upon active site binding,[29,27,30] and is responsible for narrowing the active site, functioning as a clamp to bind the FBP P_6-phosphate and, more generally, capable of accommodating binding by phosphate moieties from phosphorylated analogues of varying sizes.

A surprising structural feature in the ALDOA-**1** complex was the conformational mobility at the P_1-locus shown by **1** binding, not observed with FBP or DHAP. Upon P_1-phosphate binding by aldolase substrates, FBP or DHAP, Arg303 side chain typically undergoes a conformational change which enables it to grasp and immobilize the incoming P_1-phosphate, by forming a strong bidentate hydrogen-bond. In compound **1**, an unexpected binding mode was observed consistent with two configurations of the phosphate oxyanion at the P_1-site (Figure 1B): a major *anti* conformation with respect to the orientation of the trans-annular phosphates across the aromatic core of **1**; and a minor *syn* conformation. Only the *syn* conformer forms the anticipated salt bridge with Arg303. Population of the minor species corresponded to a refined occupancy of 0.35 ± 0.02 (average of four subunits) compared to the *anti* conformer whose occupancy was 0.65 ± 0.02 (Figure 1C - *yellow*).

The observation of two distinct binding modes for the ALDOA-**1** complex was used as a

template to design a series of novel bisphosphonate analogues, with the premise that a bisphosphonate moiety would be capable of mimicking both *syn* and *anti* phosphate positions observed in the ALDOA-**1** complex. A bisphosphonate moiety, which structurally resembles pyrophosphate, is a compelling proposition for therapeutic applications as substitution of the central oxygen atom (pyrophosphate) for carbon (bisphosphonate) procures added stability and resistance to thermal, chemical, and enzymatic degradation.[31] Bisphosphonates are a class of drugs that are primarily used for intervention in osteoporosis[32] but are also being investigated because of their inhibitory activity against several carbonic anhydrase isozymes, some of which are overexpressed in hypoxic tumors.[19,33] Here, we sought to exploit the stability of bisphosphonates by substituting the phosphate group of **1** for a bisphosphonate, generating compound **2** (PNAB) (Scheme 1). Further, to optimize targeting to the compound **1** binding site, additional topologies were sampled. Notably compounds **3** (NAB) and **4** (PBB) were synthesized either by permutation of the central naphthalene core to a benzene core (**4**) or by elimination of the second phosphate group (**3**) (Scheme 1).

Scheme 1. Synthesis of inhibitors 2 4[a]

a) synthesis of inhibitor **2**

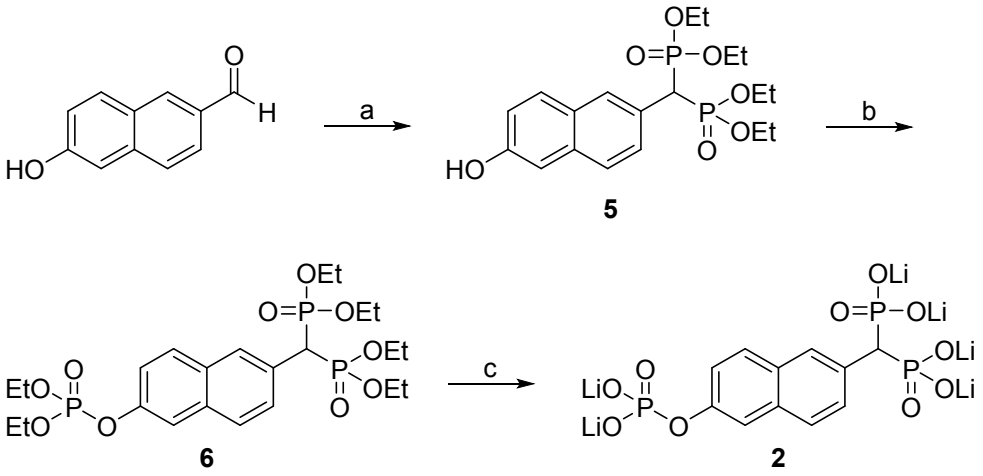

b) synthesis of inhibitor **3**

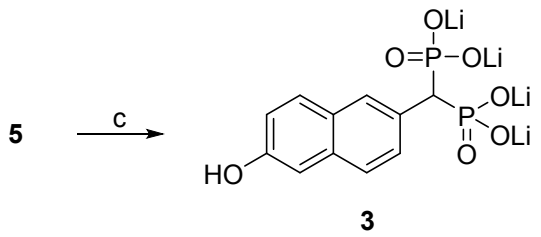

c) synthesis of inhibitor **4**

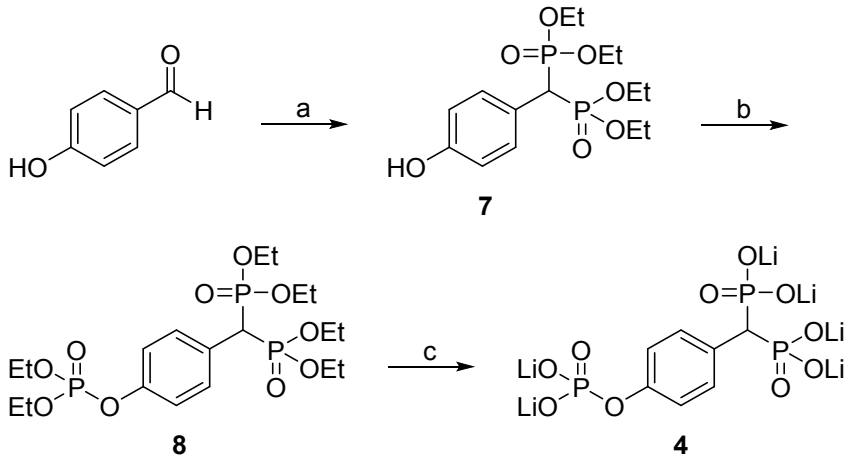

[a] Reagents and conditions: (a) $(EtO)_2P(O)H$, Na, rt, 48 h, **5** 80%, **7**[34,35] 99%; (b): $(EtO)_2P(O)Cl$, 1,4-diazabicyclo[2.2.2]octane, THF, rt, 48 h, **6** 58%, **8** 80%; (c): (i) TMSBr, 2,4,6-collidine, CH_2Cl_2, rt, 16 h, (ii) LiOH, H_2O, 80 °C, 16 h, pH 10, **2** 99%, **3** 91%, **4** 85%.

Inhibitors **2**, **3**, and **4** were prepared as represented in Scheme 1. Following reported procedures,[34,35] 6-hydroxy-2-naphthaldehyde and 4-hydroxybenzaldehyde were treated with a large excess of sodium diethylphosphite generated *in situ* to provide the respective bisphosphonates **5** and **7**[34,35] in a single step in 80% and 99% yields, respectively. The free hydroxyls of bisphosphonates **5** and **7** were phosphorylated to yield **6** and **8**, respectively, by reaction with diethyl chlorophosphate in the presence of 1,4-diazabicyclo[2.2.2]octane (DABCO) which serves both as catalyst and proton scavenger.[36] Finally, compounds **6**, **5**, and **8** were hydrolyzed under modified McKenna conditions[37] by sequential reactions with bromotrimethylsilane and 2,4,6-collidine, followed by basic treatment with 2 N LiOH, affording

inhibitors PNAB (**2**), NAB (**3**), and PBB (**4**) in 99%, 91%, and 85% yields, respectively. All inhibitors and intermediates were characterized by HRMS and ^{1}H, ^{13}C, and ^{31}P NMR spectroscopies.

High-resolution crystal structures of bisphosphonate analogues in complex with ALDOA. Native ALDOA crystals were soaked for 30 min in a solution consisting of mother liquor and a given bisphosphonate compound at final concentrations of 1 mM, 5 mM, and 20 mM for compounds **2**, **3**, and **4** respectively. Data collection and refinement statistics for the three structures are shown in Table 4 in the Experimental Section. The statistics and final resolution are indicative of the soaking conditions for each bisphosphonate: the higher concentrations used for crystal soaking with **3** and **4** to ensure adequate active site occupancy slightly impacted crystal quality, manifested by lower resolutions (2.20 Å and 2.29 Å respectively) and higher mosaicities of their intensity profiles, compared to the 1.58 Å resolution obtained for compound **2**. A control dataset for the native crystal (not shown), diffracted to 1.63 Å. All three bisphosphonates targeted the active site yet displayed surprisingly different modes of binding.

ALDOA-2 complex structure. Electron density delineating compound **2** (Figure 2A) was unambiguous and allowed for confident determination of its binding mode. The average occupancy of **2** in the four subunits was 0.78 ± 0.04. Soaking times of **2** with native crystals were limited due to degradation in crystal quality at longer soaking times. Comparison of the ALDOA-**2** complex with the ALDOA-**1** complex reveals an indistinguishable superposition of the inhibitors, notably at the P_1-site (shown in Figure 3A). In the ALDOA-**1** complex (Figure 1C), the phosphate forms 5 hydrogen bonds in either the *syn* or *anti* conformations whereas in the ALDOA-**2** complex, the bisphosphonate moiety of **2** engages in three additional hydrogen bonds with active site residues forming a network of 8 hydrogen bonds (Figure 2) (not including water molecules).

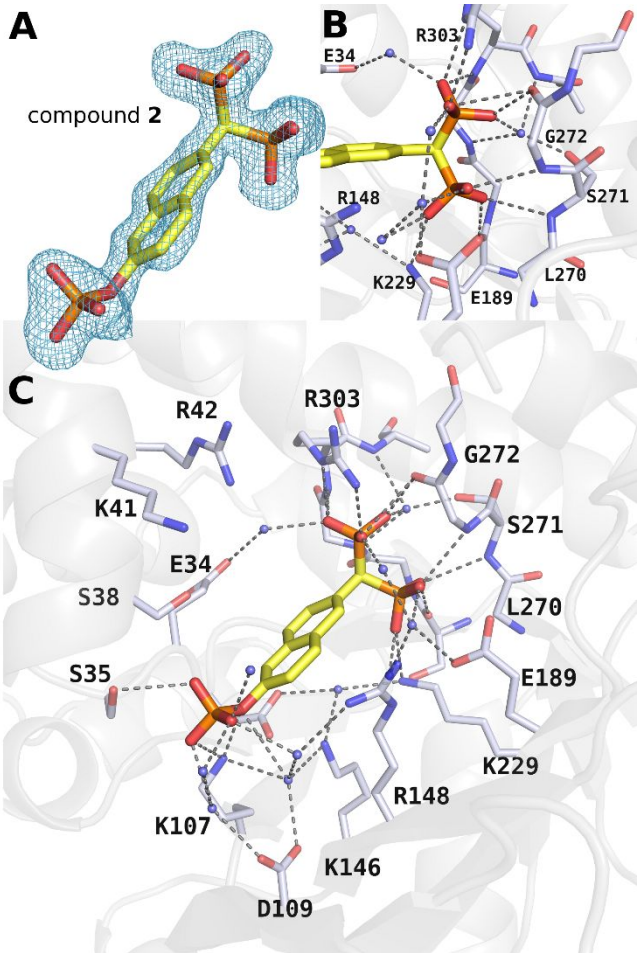

Figure 2. Crystal structure of the ALDOA-**2** complex. (A) Difference electron density calculated from a 1.58 Å simulated annealing F_o - F_c omit map encompassing compound **2** and contoured at 3.0σ. (B) Close-up of hydrogen-bonding contacts between bisphosphonate moiety and surrounding backbone atoms, side-chain atoms, and water molecules at the P_1-phosphate locus. (C) Extensive hydrogen-bonding network (*dashed lines*) between **2** and active site residues and water molecules is illustrated.

Inspection of the P_1-binding site is informative for comprehending the differences in affinity and binding kinetics in compounds **1** and **2**. Although ALDOA-**1** and ALDOA-**2** complexes appear isostructural, a notable difference was observed in the hydrogen-bonding pattern with regards to active site Ser271 (Figure 3A), where the residue which interacted with **1** no longer interacted

directly with **2** due to active site deformation by **2**. Furthermore, attachment by both complexes enabled determination of the protonation state of the phosphate and bisphosphonate moieties for binding at the P_1 locus that was based upon their interactions with surrounding backbone and side-chain atoms. In the *syn* conformation of the ALDOA-**1** complex (Figure 3B), the Gly272 backbone carbonyl engages in a hydrogen-bond with phosphate O_8 atom that is consistent with protonation of the phosphate O_8 oxyanion. Upon *syn-anti* rotational isomerization of the phosphate, the proximity of O_8 to Ser300 carbonyl implies hydrogen bond formation and also consistent with protonation of the phosphate O_8 oxyanion in the *anti* conformation. This hydrogen-bonding pattern implies mono-protonation of the bound P_1 phosphate oxyanion. In the ALDOA-**2** complex, Ser271 shifts to the rear of the active site (by 1.7 Å compared to ALDOA-**1**) to accommodate bisphosphate binding and is replaced by W1, which donates two hydrogen bonds to the bisphosphonate moiety (Figure 3C – *green dashes*). W1 also accepts hydrogen bonds from surrounding active site atoms (Gly302 N_H and Ser271 O_H). For this binding geometry, O_{17} interacts with Ser300 carbonyl while O_{21} interacts with Gly272 carbonyl indicating binding by **2** is consistent with protonation of each phosphonate moiety (i.e. dibasic bisphosphonate). Displacement of Ser271 with respect to the native enzyme reflects active plasticity in accommodating binding by compounds **1** and **2**.

Prior to synthesis of compound **2**, the naphthalenic derivative **1** represented the most potent reversible competitive inhibitor of the rabbit muscle aldolase-catalyzed reactions. The design of compound **1** was based on two chemical features useful for enhancing active site binding. Protection experiments had shown that the active site binding embodied two distinct phosphate binding sites: a higher affinity site – the P_1-site; and a lower affinity site – the P_6-site making binding by compounds with suitable spanning phosphate groups to both sites highly specific.[28,38] A second distinguishing feature of potent aldolase inhibitors (0.1 – 1.0 μM range) were those

possessing aromatic moieties.[16] The rigid structure imposed by the aromatic rings compared to a flexible compound such as hexanediol 1,6-bisphosphate (K_i = 25 μM) suggests that a smaller configurational entropy loss upon active site binding by a rigid aromatic compound may underpin the observed differences in binding affinity to aldolase.[39] The additional feature of a bisphosphonate moiety in compound **2** took advantage of the cryptic phosphate binding site at the P_1 site to enhance binding affinity. Modifications were made of the bisphosphonate derivative **2** that were designed to explore additional conformational space in the aldolase active site. First, the synergy between the two phosphate loci was probed by replacing the phosphate group with a hydroxyl group (**3**), also providing an indication of the significance of the bisphosphonate moiety towards potency. Then, to assess the sufficiency of the naphthyl core in spanning the phosphate loci, a shorter aromatic core was introduced - a phenyl group (**4**).

ALDOA-3 complex structure. The crystal structures of ALDOA-**3** and ALDOA-**4** are shown in Figure 4. The binding mode of **3** and **4** are noticeably different than **2**. First, their bisphosphonate moieties do not bind at the P_1-site. The bisphosphonate in the ALDOA-**3** structure (Figure 4A) points towards the outside of the active site cavity and forms hydrogen bonds with the side chains of surrounding residues (Ser45, Lys311, Arg303, Arg42). Further, the naphthyl moiety of **3** is conjugated to Arg42 via a cation-π interaction, a highly stabilizing interaction.[40,41] The distance between the guanidinium group and the naphthalene ring in all four subunits is 3.48 ± 0.10 Å, consistent with reported cation-π interactions for arginine.[40,42] The interaction is further stabilized by a salt bridge that forms between Arg42 and the bisphosphonate oxygens. Also, Arg303 side-chain carbon atoms align on the distal sides of **3**, producing a stabilizing hydrophobic environment for the naphthyl moiety. The distal O_H group of **3** is anchored by a hydrogen bond with the Glu34 carboxyl.

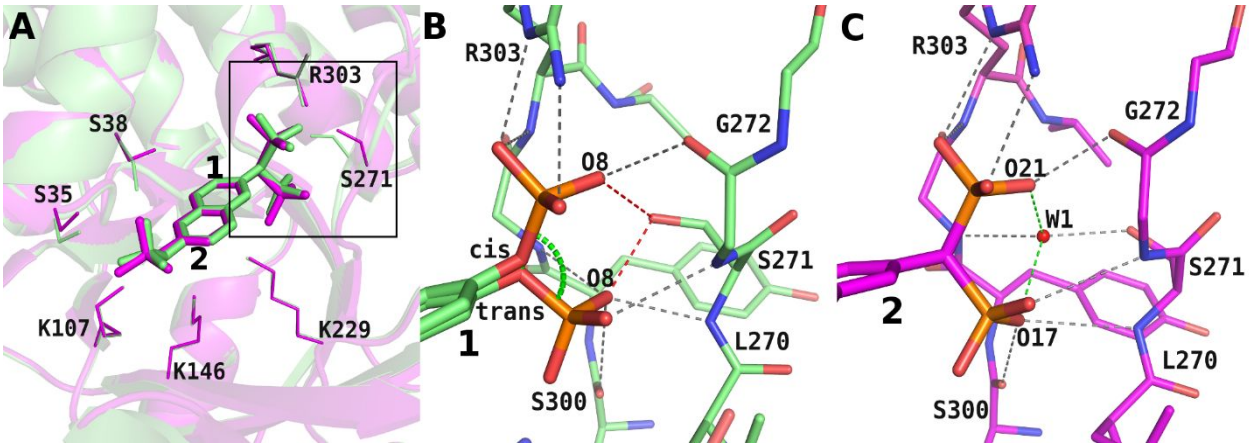

Figure 3. Superposition of the ALDOA-**1** and ALDOA-**2** complexes and interactions at the P_1-site. (A) The structures of ALDOA complexed with **1** (*green*) and **2** (*magenta*) were superposed in PyMol to illustrate the structural similarities of their binding modes (r.m.s.d. = 0.21 Å for alignment of C_α atoms in subunit A). One notable difference was observed for Ser271, shown in the inset. (B) Hydrogen-bonding network (*grey dashes*) of ALDOA-**1** complex at the P_1-binding site is illustrated for the *syn* and *anti* conformers. The *syn-anti* rotational isomerization is depicted by a *green arc*. The proximity of the Gly272 carbonyl to the phosphate O_8 of *syn*-**1** (2.89 ± 0.14 Å) implies protonation of the phosphate O_8 and indicates proton donation by Ser271 O_H (*red dashes*) to O_8 (*syn*: 2.80 ± 0.08 Å; *anti*: 2.65 ± 0.20 Å). Further, proximity of *anti*-**1** phosphate O_8 to the Ser300 carbonyl (3.00 ± 0.10 Å) is consistent with protonation of O_8. (C) In the ALDOA-**2** complex (*magenta*), the vicinal Gly272 and Ser300 backbone carbonyls also indicate protonation of the partnered oxygens on the bisphosphonate (O_{21} – 2.76 ± 0.06 Å; O_{17} – 2.82 ± 0.01 Å, respectively). Ser271 side-chain shifts to the rear, making room for a water molecule (W1) that donates hydrogen bonds to O_{17} (3.22 ± 0.04 Å) and O_{21} (2.31 ± 0.13 Å) (*green dashes*), and accepts hydrogen bonds from Ser271 side-chain O_H and Gly302 backbone N_H.

A second binding site for **3** was identified near the P_6-locus but electron density was only visible for the bisphosphonate group (seen in Figure 4A), consistent with purity assessments showing no indication of free bisphosphonate, and indicative of positional disorder of the naphthyl group at the second binding site.

The hydrophobic pocket used by **3** is a recognized binding locus for aldolase-binding partners, including the C-terminal peptide of the actin nucleation-promoting factor WASP and the LC4 domain of SNX9, a key regulator of endocytosis in cellular cargo transportation, which both intercalate a tryptophan indole ring between Arg42 and Arg303.[43,44] A novel naphthyl phosphate-based inhibitor of aldolase (NASEP) identified from the WASP study was competitive for active site binding and had a K_i of 0.1 mM. Comparison of the ALDOA-**3** complex with the ALDOA-NASEP complex (PDB id: 2OT1) (illustrated in Figure S2) revealed a difference of ~81° in the angle of insertion of the naphthyl group with respect to the primary axis of the NASEP naphthyl ring. The stabilizing cation-π interaction is also observed in the ALDOA-NASEP complex and appears to be a driving force for binding at this locus but is insufficient alone as native ALDOA crystals soaked in saturating tryptophan in the crystallization buffer (6 mM L-tryptophan) did not reveal evidence of tryptophan active site binding.[43] The ancillary hydrogen bonds formed between inhibitor oxygens and basic active site residues are therefore required to promote active site binding at this locus.

ALDOA-4 complex structure. The ALDOA-**4** complex (Figure 4B) revealed a novel mode of binding different from the previous bisphosphonate compounds. The bisphosphonate moiety of **4** is isostructural with the secondary binding site identified in the ALDOA-**3** complex. This site is located near the P_6-binding locus: one phosphonate group of **4** contacts several active site residues (Ser35, Ser38 and Lys107); the second phosphonate is stabilized by hydrogen-bonding to Lys146.

The phosphate group forms an electrostatic interaction with Arg303. To accommodate the binding mode of **4** and avoid clashing with the benzene group, Arg42 folds into the hydrophobic pocket described above for **3**.

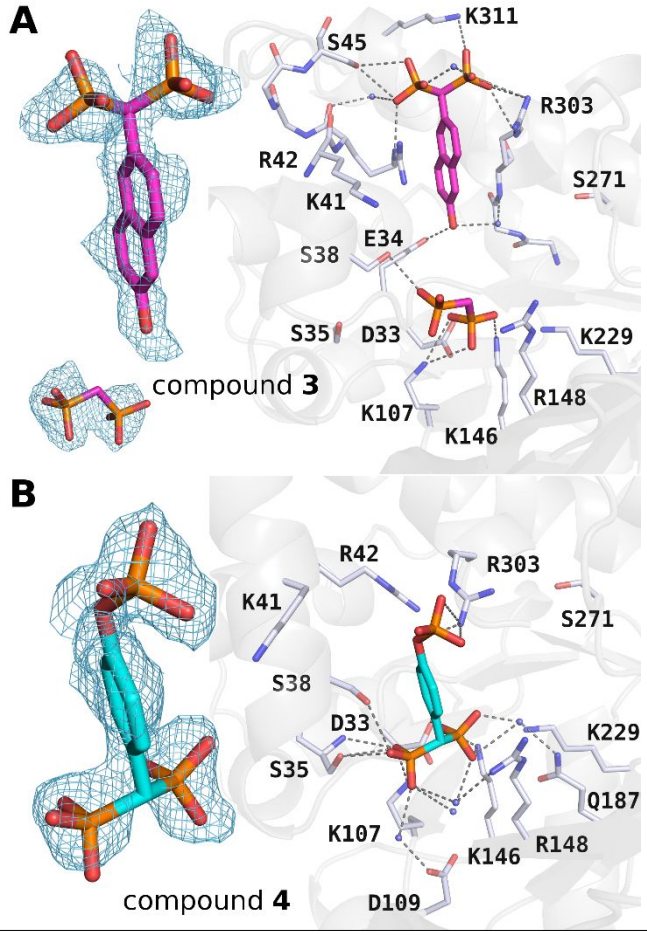

Figure 4. Crystal structure of ALDOA in complex with compounds **3** and **4**. (A) Difference electron density calculated from a 2.20 Å $2mF_o - DF_c$ Feature Enhanced Map (FEM) showing compound **3** and contoured at 1.0σ. Noteworthy is the cation-π interaction involving Arg42 and the naphthalene moiety of compound **3** and the hydrophobic interaction with the side-chain of Arg303, shown on the right-panel. (B) Difference electron density calculated from a 2.29 Å $2mF_o - DF_c$ FEM comprising compound **4** and contoured at 1.0σ. Compound **4** binding mode is different from other bisphosphonates. The hydrogen-bonding networks shows the bisphosphonate moiety contacting the P_6-phosphate binding locus involving Ser35 and Lys107.

Inhibition kinetics of the bisphosphonate inhibitors. The potency of the bisphosphonate analogues **2, 3** and **4** were investigated by inhibition kinetics using previous buffer conditions (see Experimental Section). Potency of **2** was evaluated using IC50 assays, summarized in Table 1 Indication that **2** exhibited slow-binding behavior arose from IC50 experiments with different pre-incubation periods of the enzyme with **2** in solution. An IC50 value of 0.67 ± 0.07 μM was measured with no pre-incubation period which decreased 10-fold to an IC50 of 0.060 ± 0.008 μM with a pre-incubation of 90 min. To determine the nature of the slow-binding behavior by **2**, time-dependent inhibition by **2** was assessed using the method first described by Morrison and Walsh (see Experimental Section for details).[45] Briefly, in the presence of classical competitive inhibitors, product formation remains linear prior to substrate depletion. With slow-binding inhibitors, inhibition exhibits a two phase relationship: an initial burst in product formation (v_o) corresponding to an apparent first-order loss (k_a) of activity followed by a slower steady state rate in product formation (v_s) where progress curves becomes asymptotic to the v_s. Equations 2 – 4 described in the Experimental Section were used to extract inhibition constants and are reported in Table 2 (direct and linearized plots are reported in Figure S3). An overall inhibition constant K_i* of 38 ± 2 nM was determined. The off-rate constant of the slow-binding event (k_{-4}) was 6-fold slower than the on-rate (k_{+4}) and predicts a turnover of inhibited complex (EI*) consistent with the long pre-incubation periods required to observe full inhibition in IC50 assays. The K_i for compound **2** was 280 ± 10 nM which is virtually identical to the K_i of compound **1** of 280 ± 30 nM, coherent with the isostructural binding mode of compounds **1** and **2**. Binding of **1** and **2** at the P_6-site is quasi-isostructural, indicating that binding features at the P_1-site likely account for the difference in overall affinity. The 8 hydrogen bonds for **2** at the P_1-site with surrounding residues compared to 5 hydrogen bonds for **1** affords a greater enthalpic binding energy for **2**, yet the entropic penalty

for binding of **1** is smaller due to the *syn-anti* rotational isomerization at the P_1-site. However, binding of **2** provokes the expulsion of one additional highly ordered water molecule (W1) compared to **1** which is entropically favorable, and suggesting a higher overall affinity of **2** for aldolase.

Table 1. IC50 values for aldolase inhibition by **2** measured for varying pre-incubation periods.

Pre-incubation period (min)	IC50 (μM, pH 7.5) [a]
0	0.67 ± 0.07
10	0.17 ± 0.02
30	0.13 ± 0.01
90	0.060 ± 0.008
180	0.068 ± 0.004

[a] Measured in Tris-Acetate buffer (pH 7.5) with 10 μM FBP using activity assay described in Experimental Section.

Table 2. Kinetic parameters describing the slow-binding inhibition of aldolase with **2**.

Parameter	Value [a]
V_m (U/mg)	11.7 ± 0.2
K_m (μM)	2.7 ± 0.3
K_i (μM)	0.28 ± 0.01
k_{-4} (min^{-1})	0.010 ± 0.002
k_{+4} (min^{-1})	0.064 ± 0.002
K_i* (μM)	0.038 ± 0.002

[a] Values were calculated using the slow-binding model described in the Experimental Section. Direct and linearized Dixon plots are shown in Figure S3.

Dual competitive inhibition of aldolase by 3. Compound **3** did not show any changes in IC50 with different incubation times and was analyzed in terms of competitive inhibition as kinetic model. Given the presence of a second binding site by **3** in the active site, we applied a semi-generalized formulation for single-enzyme multiple inhibition using two reversible linear inhibitors, as previously reported and described by equation 5 (details in Experimental Section).[46] The inhibition constants for the two binding sites yielded values of 13 ± 3 μM and 9 ± 1 μM

(reported in Table 3; inhibition kinetics are shown in Figure S4). Additional enthalpic contributions afforded by 3 extra hydrogen bonds in the ALDOA-**3** complex (7 hydrogen bonds) compared to ALDOA-NASEP (4 hydrogen bonds) is consistent with tighter binding of **3** compared to the similar NASEP inhibitor (K_i = 0.1 mM). Further, the naphthol O_H group has an important role in binding affinity as it anchors the naphthalene to Glu-34 (Figure 4A), a contact not formed in the ALDOA-NASEP complex (Figure S2).

Competitive inhibition of aldolase by 4. Compound **4** showed no evidence for slow binding behavior and exhibited classical competitive inhibition consistent with the observation in the ALDOA-**4** complex showing active site tethering at the P_6-phosphate site. The inhibition constant has a value of 42 ± 5 μM (Table 3; inhibition kinetics are illustrated in Figure S5).

Table 3. Inhibition mode and constants for inhibitors **1 – 4**.

Inh	Mode	K_i (μM)	K_i* (μM)
1	*Competitive* [a]	0.280 ± 0.030	-
2	*Slow-binding* [b]	0.280 ± 0.010	0.038 ± 0.002
3	Dual Compet. [c]	13 ± 3	9 ± 1
4	Competitive [d]	42 ± 5	-

[a] Previously reported[18]; [b] Calculated using slow-binding inhibition described in Experimental Section; K_i* is the overall inhibition constant; [c] Calculated using dual linear competitive inhibition described in Experimental Section; Here, K_i and K_i* represent the inhibition constants for the two binding sites in the aldolase active site; [d] Calculated using classical competitive inhibition kinetics: direct and double-reciprocal plots are shown in Figure S3 – Figure S5. Inh, Inhibitor.

Slow-binding inhibition mechanism. Compounds **1** and **2** provided an ideal opportunity to investigate the structural features responsible for their different modes of inhibition. Both compounds occupy the same binding sites yet differ in that **2** displays slow binding inhibition while **1** does not. Earlier work had shown that substitution of a phosphate group on **1** with an aldehyde (1,6-dihydroxy-2-naphthaldehyde - HNA-P) results in Schiff base formation between Lys107 and HNA-P.[18] It was suggested that the rate of covalent bond formation was responsible

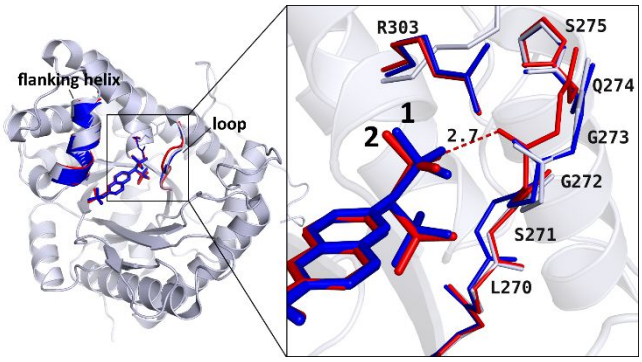

Figure 5. Active site dynamics upon aldolase-binding of **1** and **2**. ALDOA-**1** (*blue*), ALDOA-**2** (*red*) and native ALDOA (*grey*) (PDB id: 1ZAH) were aligned using ProSMART, identifying two regions with significant conformational differences (the flanking helix and the flexible active site loop). The inset depicts a close-up of the flexible loop, comparing the differences between all three structures. In ALDOA-**2,** the loop undergoes significant movement of residues 272-275 (r.m.s.d. of 0.66 ± 0.03 Å) towards the active site cleft, affording a hydrogen bond between Gly272 and the bisphosphonate not present in ALDOA-**1**, where the loop undergoes minimal displacement with respect to ALDOA (r.m.s.d. of 0.23 ± 0.02 Å). For illustration purposes, the side-chains were omitted from the loop.

for the slow binding reaction. However, the slow-binding mechanism of aldolase bisphosphonate inhibitors does not entail formation of a covalent adduct. In order to identify hot spots in the structure that may explain the slow-binding origin of **2**, the ALDOA-**1** and ALDOA-**2** complexes were aligned to native ALDOA (PDB id: 1ZAH) using the ProSMART algorithm.[47]

Overall global root mean square deviations (r.m.s.d. based on Cα atoms) were comparable (ALDOA-**1**-native: 0.31 ± 0.01 Å; ALDOA-**2**-native: 0.23 ± 0.02 Å) and localized to two main regions: 1) the active site flanking helix comprising residues 34-45; and 2) a loop comprising residues 269-275 (Figure 5). The conformational changes induced in the flanking helix upon FBP binding upon active site binding have not been associated with a slow binding mechanism in case

of inhibitors such as the tagatose-bisphosphate diastereoisomer (K_i = 120 ± 10 μM).[27] The conformational changes for the loop comprising residues 269-275 were 0.46 ± 0.02 Å in ALDOA-**2** compared to ALDOA-**1** of 0.31 ± 0.01 Å (r.m.s.d. for residues 268-276 from alignment of Cα atoms) with respect to the native structure ALDOA. The local r.m.s.d. of the same loop for the FBP bound structure (PDB id: 1ZAI) was 0.31 ± 0.02 Å. The local r.m.s.d. becomes even greater for ALDOA-**2** using only residues 272-275 that exhibit the greatest movement (ALDOA-**2** vs native: 0.66 ± 0.03 Å and ALDOA-**1** vs native: 0.23 ± 0.02 Å). We speculate that movement by this loop to accommodate the bisphosphonate moiety in **2** may be the structural basis for the slow-binding inhibition. Indeed, shown in Figure 5, the greatest backbone movement incurred by residues 272-275 in ALDOA-**2** (Figure 5 – *red*) implicated the displacement of Gly272 carbonyl towards the bisphosphate moiety, producing a strong hydrogen-bond (2.76 ± 0.06 Å). This movement is absent in ALDOA-**1** and where side chain displacements were limited to a single residue, Ser-271. We also considered the contribution of the protonation state of the bisphosphonate in the slow binding inhibition.

Ionization state of bisphosphonates. Bisphosphonates have four ionizable species (monobasic, p*K*a1=1.3; dibasic, p*K*a2=3.2; tribasic, p*K*a3=6.9; tetrabasic, p*K*a4~11).[48,49] The protonation state of **2** was inferred from the hydrogen bonding network of the ALDOA-**2** complex (shown in Figure 3C) and corresponded to a mono-protonation state for each phosphonate group which is consistent with a dibasic species as the dominant protonated state between pH 3.2 – 6.9, according to the p*K*a values listed above. At pH 7.5, the conditions used for the inhibition kinetics implies that both dibasic and tribasic species of **2** are present in solution and only the dibasic species would have the protonation state competent for binding. Preferential binding by the dibasic species implies even tighter binding by **2** when the pH dependence of this species is considered. At pH 7.5, the

population of the dibasic species represents ~20% of the ionizable species and binding constants when corrected for this population correspond to apparent K_i and K_i* values of ~56 nM and ~7.6 nM, respectively.

Minimal requirements of high-affinity binders. Fundamental to all known high-affinity aldolase binders is the inclusion of phosphate oxyanions that afford interactions with the highly basic active site, which includes 5 lysine and 3 arginine residues. The apparent promiscuity of the compound binding modes in the active site may in part be due to the positively charged landscape making up the active site that is not very heterogeneous in terms of charge distribution (see Figure 1A) and hence would not enforce strongly similar binding modes on the bisphosphonate derivatives. Comparison of the structural and kinetic data does however provide guiding principles that can be applied to the next generation of high-affinity binders. First, the weaker binding bisphosphonates compounds **3** and **4** compared to compound **2** clearly demonstrated the importance of the P_6-site for high affinity binding. Substitution of a phosphate in **2** for a hydroxyl in **3** had a dramatic effect on the binding mode and inhibition constant, consistent with the shorter span of compound **3** to simultaneously contact both P_1- and P_6-sites. This was corroborated by **4**, whose benzene core had a shorter span than the naphthalene core of **2** (~2.2 Å shorter). The minimum span required to contact the P_1- and P_6-sites is ~9 Å, which is possible with **2** (9.7 Å) however, **4** has a span of ~7.5 Å, insufficient to contact both phosphate binding loci. Attachment to not only the P_1-binding locus but also to the P_6-binding locus is synergistic and is an important consideration in the design of high affinity phosphorylated binders.

A similar trend that inhibitors capable of simultaneously satisfy binding to both phosphate binding loci exhibit tighter binding can be drawn from a study of linear bisphosphorylated inhibitors used as structural analogs of FBP for probing the active site of aldolase.[50] K_i values for

propanediol-, butanediol-, pentanediol-, and hexanediol-bisphosphate inhibitors were determined to be 120, 55, 29, and 25 μM respectively. Modelling inhibitors into the active site, using the P_1- and P_6-binding locus of FBP as guides, indeed found the phosphate moieties of pentane- and hexanediol-bisphosphate could readily satisfy binding to both loci without steric collisions whereas the propanediol- and butanediol-bisphosphate are unable to span the $P_1 – P_6$ distance.[50,51]

Inhibition of aldolase *in vivo* by a bisphosphonate inhibitor. Finally, we performed *in vivo* inhibition assays in order to test cellular proliferation in the presence of the most potent bisphosphonate inhibitor, **2**. The results of the dose response assay shown in Figure 6 indicate that increased inhibitor concentration progressively inhibits proliferation of HeLa cells (Figure 6A), yet surprisingly with no effect on cellular proliferation at any tested concentration in HEK293 cells (Figure 6B). Furthermore, there was no growth inhibition of HeLa cells with the least potent bisphosphonate, **4**, under identical incubation conditions (Figure 6C). The decrease of ~50% after 72 h of incubation by **2** at 50 μM ($p \leq 0.01$) is consistent with an EC50 ~50 μM for **2**. Incubation of cell growth ~ 30% by 72 h ($p \leq 0.01$) at the lower concentration of 10 μM of compound **2** supports an EC50 estimate of 50 μM.

The charged nature of phosphate groups greatly impedes endogenous phosphate-derivatives from escaping the cell, and renders exogenous phosphate-derivatives highly impermeable to entry across the membrane.[52] Indeed, **2** displayed *nano*-molar inhibition *in vitro*, while only exhibiting inhibition of cellular proliferation in the *micro*-molar range suggesting that the membrane permeability of **2** may be an issue given the presence of one phosphate group and two phosphonate moieties on **2**. Surprisingly, phosphorylated compounds such as FBP at high doses have been shown to display a protective effect in inflammation,[53,54] and exert their therapeutic effect by diffusion through membrane bilayers in a dose-dependent manner with no loss in cell viability and

a transport efficiency of ~5% for 20 mM extracellular dose of FBP.[55] From this transport efficiency, the corrected K_i for **2** would predict an EC50 of ~ 5 μM in the dose response shown in Figure 6A. The presence of an additional charged phosphate moiety on **2** compared to FBP would likely further reduce transport efficiency which is not inconsistent with the observed EC50 ~50 μM.

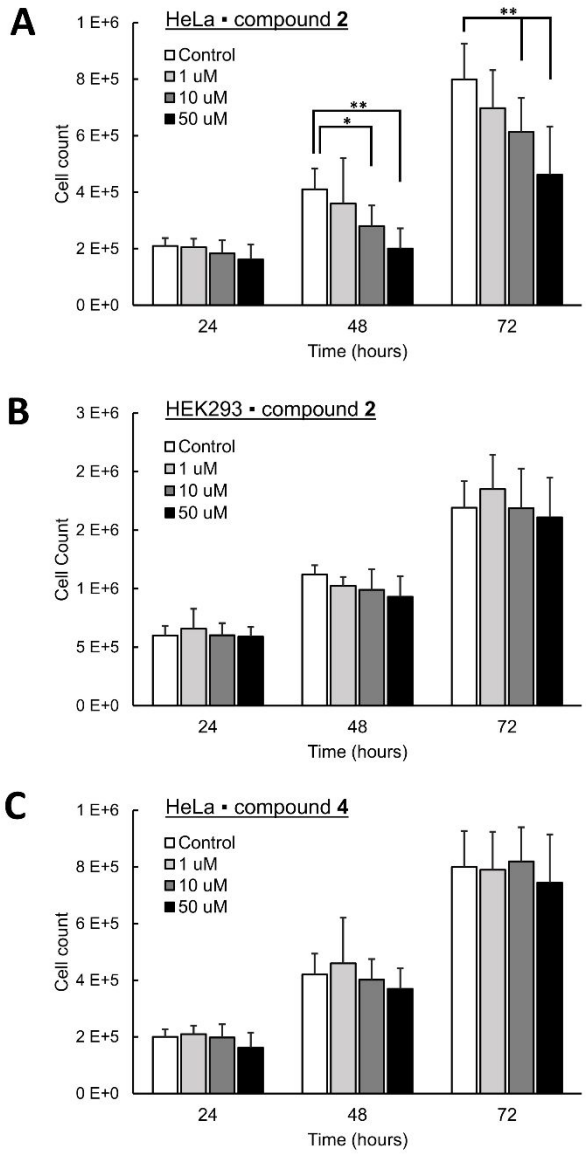

Figure 6. Cell growth inhibition assay. (A) Graph shows cell count as a function of inhibitor concentration with HeLa cells. Cells were incubated for periods of 24, 48, and 72 h with inhibitor. Cell count was determined by Trypan blue exclusion and hemocytometer. The same is shown in (B) for HEK293 cells. (C) The least potent bisphosphonate, compound **4**, served as a control treatment for HeLa cells. * $p \leq 0.05$; ** $p \leq 0.01$ (Student's two-tailed *t*-test). Data are from at least three independent experiments (standard deviations are shown as error bars).

Cellular targeting of glycolytic aldolase by **2** is thus not inconsistent with the proliferation data. Lessor dependence on glycolytic flux in normal phenotypes would afford selectivity as inhibition of glycolytic flux in hyperglycolytic phenotypes by **2** such as in cancer cells or protozoan infections would be detrimental to their proliferation. The fact that the dose response assay for **4**, shown in Figure 6C, does not reduce cell viability (Figure 6B), and that **4** inhibits aldolase with 150-fold lower efficacy compared to **2** indicating a very large EC50 suggests that the aldolase inhibition of cellular proliferation may have selectivity by inhibiting proliferation of cancerous phenotypes without effect on normal ones. In hyperglycolytic cells where glycolysis is the main source of energy and biomass production (Warburg effect), targeting glycolysis via aldolase inhibition has been shown to be a viable strategy for inhibiting cellular proliferation.[56] Upregulation of ALDOA has recently been identified as an oncogene in a subpopulation of patients with highly metastatic pancreatic cancer[11] and an overall increase in aldolase gene transcripts was observed for AML (acute myeloid leukemia) cells upon stromal interaction.[57]

Implications for Drug Design. From this study, functional groups, including phosphate, bisphosphonate, and naphthyl moieties of bisphosphonate inhibitors are important constituents for tight binding and represent a template for the design of future inhibitors. The highly basic nature of the aldolase active site is amenable to binding by phosphate oxyanions and drives the binding of the tested bisphosphonates to a number of different basic loci. In order to target binding to specific loci (i.e. P_1 & P_6) and afford the greatest potency, the following essential design features should be taken into consideration: 1) ability by compound phosphates to bind both P_1- and P_6-loci; and 2) retention of a rigid scaffold (naphthyl moiety) to reduce the entropic cost of binding. Using this template, we can envisage the addition of functional groups based on the proximity to surrounding residues to yield a library of high-affinity inhibitors that can serve as leads for future

studies. For example, the binding locus of compound **3** at the hydrophobic pocket formed by Arg42 and Arg303 could be exploited by the addition of an aromatic group to a phosphonate moiety of **2**. To improve stability, a phosphonate moiety at the P_6-position would ensure stability against tyrosine phosphatases. The loss of a stabilizing hydrogen bond with Lys146 could be restored with a fluorine substituent on the phosphonate carbon. Also, the ionization state of the bisphosphonate should be considered to maximize biological activity at physiologically relevant pHs. Electronegative substituents on phosphonate carbons (e.g. fluorination) are known to lower the p*K*a of phosphonates, promoting the fully ionized form at neutral pH.[58,59] However, since **2** is competent for binding in the di-protonated bisphosphonate form, a methyl substituent may promote the dibasic bisphosphonate species at neutral pH by increasing p*K*a3.

The presence of phosphate groups has been problematic in drug design because of the poor ability by phosphate monoesters to penetrate cell membranes. These impediments can be circumvented by synthesizing a prodrug that masks the phosphate charges using a protecting group that can be enzymatically converted into the active phosphate monoester form once the prodrug has been internalized.[60–66] A number of approaches have been developed capable of yielding compounds with such "drug-like" properties.[52] Foremost was the modification of the phosphate group such that the inhibitor could diffuse through membranes and typically involved charge neutralization via chemical derivatives to form neutral esters(s) with the phosphorus-derived oxygen(s). The protective groups allow permeation of the prodrug into the cells and can be efficiently removed by endogenous esterases, which restore the charge and biological activity. This approach was successfully implemented with a bisphosphonate inhibitor of inositol monophosphatase, where initially, poor membrane permeability was noted, but was rescued by using a tetrapivaloyloxy-methyl ester prodrug that retained biological activity after removal of the

chemical modification by endogenous esterases.[67,68]

EXPERIMENTAL SECTION

General Methods. All chemical reagents were of analytical grade and used without further purification. CH_2Cl_2 and THF were dried on molecular sieves and used immediately. Flash chromatography was performed using silica gel (35-70 µm, Merck). Concentration of solutions was performed under diminished pressure at temperature < 40 °C using a rotary evaporator. All air- and moisture-sensitive reactions were performed under an atmosphere of argon. Analytical TLC was performed using silica gel 60 F_{254} pre-coated aluminum plates (Merck). Spots were visualized by treatment with ninhydrin revelator followed by heating and/or by absorbance of UV light at 254 nm. NMR spectra were recorded at 297 K in $CDCl_3$ or D_2O with Bruker DRX400 (^{1}H at 400.13 MHz and ^{13}C at 100.62 MHz) and DRX300 (^{1}H at 300.13 MHz, ^{13}C at 75.47 MHz, and ^{31}P at 121.50 MHz) (shown in Figures S6 – S8). Chemical shifts are reported in ppm (δ) and coupling constants in Hz (J_{ij}). ^{1}H NMR spectra were referenced to internal residual chloroform (δ 7.26) and HOD (δ 4.80) for solutions in $CDCl_3$ and D_2O, respectively. ^{13}C NMR spectra were referenced to solvent for solutions in $CDCl_3$ (δ 77.0) and to dioxane (δ 67.4) for solutions in D_2O. ^{31}P NMR spectra were referenced externally to 85% aq H_3PO_4 (δ 0.0). In most cases, COSY, HSQC, and/or DEPT135 NMR spectra were recorded for assigning resonances. Melting points were determined by using open capillary tubes with a Buchi™ M-560 apparatus and are corrected. Low-resolution mass spectrometry (MS) and high-resolution mass spectrometry (HRMS) analyses were performed by electrospray with positive (ESI+) or negative (ESI-) ionization mode on a Bruker micrOTOF. The purity of all inhibitors (≥ 95%) was determined by HPLC analysis (shown in Figure S9). HPLC analysis was run on an Agilent 1260 Infinity system equipped with a Zorbax RX-C18, 3.5 µm (4.6 x 100 mm), using isocratic elution mode H_2O/MeCN 70/30 for **2-4** and 55/45 for **5-8** over 10 min run time at flow rate 0.6 mL/min and UV detection at 254 nm.

Synthesis and Characterization of inhibitors and intermediates.

Lithium 6-(Bis(phosphonato)methyl)naphthalen-2-yl Phosphate 2. Compound **6** (164 mg, 0.29 mmol, 1.0 equiv) was dissolved in anhydrous CH_2Cl_2 (6 mL) and the solution was cooled to 0 °C. 2,4,6-Collidine (0.58 mL, 4.36 mmol, 15 equiv) and bromotrimethylsilane (0.69 mL, 5.22 mmol, 18 equiv) were added dropwise and the reactant mixture was stirred overnight at rt under argon. Once the reaction was completed (monitoring by ^{31}P NMR), it was poured into toluene (15 mL) and evaporated under reduced pressure (3 times). The crude material was treated with 2 N LiOH (1.3 mL) overnight at 80 °C and then acetone was added to precipitate the product. The light brown solid produced was dissolved in 5 mL of distilled H_2O and washed with $CHCl_3$ (2 x 25 mL), precipitated with acetone (25 mL) and collected by centrifugation (10 min, 3000 rpm) to yield **2** as a pale orange solid (114 mg, 91%). Mp > 400 °C. ^{1}H NMR (400 MHz, D_2O) δ 7.83-7.54 (m, 5H, 5 x H_{Ar}), 7.30 (m, 1H, H_{Ar}), 3.28 (t, 1H, J = 20.0 Hz, P_2CH). ^{13}C NMR (100 MHz, D_2O) δ 150.6 (d, J = 7.0 Hz, C_{Ar}-OP), 135.9 (t, J = 7.0 Hz, C_{Ar}), 131.9 (C_{Ar}), 129.9 (CH_{Ar}), 129.5 (C_{Ar}), 128.6 (CH_{Ar}), 127.6 (CH_{Ar}), 125.9 (CH_{Ar}), 121.3 (d, J = 4.0 Hz, CH_{Ar}), 115.2 (d, J = 3.0 Hz, CH_{Ar}), 50.5 (t, J = 112.0 Hz, CH). ^{31}P NMR (121 MHz, D_2O, 85% H_3PO_4) δ 18.60 (2 P), 0.39 (P). HPLC T_r = 1.39 (98% rel. area). MS (ESI-) $[M - 6Li + 5H]^-$ 397.0, $[M - 4Li + 3H]^-$ 409.0. HRMS (ESI-) calcd for $C_{11}H_{10}O_{10}P_3Li_2$ $[M - 4Li + 3H]^-$ 408.9807, found 408.9802.

Lithium ((6-hydroxynaphthalen-2-yl)methylene)bis(phosphonate) 3. Compound **5** (100 mg, 0.23 mmol, 1.0 equiv) was dissolved in anhydrous CH_2Cl_2 (5 mL) and the solution was cooled to 0 °C. 2,4,6-Collidine (0.31 mL, 2.32 mmol, 10 equiv) and bromotrimethylsilane (0.37 mL, 2.78 mmol, 12 equiv) were added dropwise and the reactant mixture was stirred overnight at rt under argon. Once the reaction was completed (monitoring by ^{31}P NMR), it was poured into toluene (15 mL) and evaporated under reduced pressure (3 times). The crude material was treated with 2 N

LiOH (0.7 mL) overnight at 80 °C and then acetone was added to precipitate the product. The light brown solid produced was dissolved in 5 mL of distilled H_2O and washed with $CHCl_3$ (2 x 25 mL), precipitated with acetone (25 mL) and collected by centrifugation (10 min, 3000 rpm) to yield **3** as a pale orange solid (79 mg, 99%). Mp > 400 °C. ^{1}H NMR (300 MHz, D_2O) δ 7.63-7.40 (m, 4H, 4 x H_{Ar}), 6.87-6.78 (m, 2H, 2 x H_{Ar}), 3.15 (t, J = 21.0 Hz, 1H, P_2CH). ^{13}C NMR (75 MHz, D_2O) δ 163.3 (C_{Ar}OH), 133.7 (C_{Ar}), 131.7 (C_{Ar}), 129.2 (CH_{Ar}), 128.7 (CH_{Ar}), 127.5 (CH_{Ar}), 125.6 (C_{Ar}), 123.8 (CH_{Ar}), 123.3 (CH_{Ar}), 109.4 (CH_{Ar}), 49.8 (t, J_{CP} = 113.3 Hz, CH). ^{31}P NMR (121 MHz, D_2O, 85% H_3PO_4) δ 18.83 (2 P). HPLC T_r = 1.53 (96% rel. area). MS (ESI+) $[M – Li + 2H]^+$ 337.0, $[M + Na]^+$ 365.1. HRMS (ESI-) calcd for $C_{11}H_{11}O_7P_2$ $[M – 4Li + 3H]^-$ 316.9980, found 316.9984.

Lithium 4-(Bis(phosphonato)methyl)phenyl Phosphate 4. Compound **8** (150 mg, 0.29 mmol, 1.0 equiv) was dissolved in anhydrous CH_2Cl_2 (6 mL) and the solution was cooled to 0 °C. 2,4,6-Collidine (0.58 mL, 4.36 mmol, 15 equiv) and bromotrimethylsilane (0.69 mL, 5.22 mmol, 18 equiv) were added dropwise and the reactant mixture was stirred overnight at rt under argon. Once the reaction was completed (monitoring by ^{31}P NMR), it was poured into toluene (15 mL) and evaporated under reduced pressure (3 times). The crude material was treated with 2 N aq LiOH (1.3 mL) overnight at 80 °C and then acetone was added to precipitate the product. The light brown solid produced was dissolved in 5 mL of distilled H_2O and washed with $CHCl_3$ (2 x 25 mL), precipitated with acetone (25 mL) and collected by centrifugation (10 min, 3000 rpm) to yield **4** as a white solid (95 mg, 85%). Mp > 400 °C. ^{1}H NMR (300 MHz, D_2O) δ 7.24 (d, J = 6.0 Hz, 2H, H_{Ar}), 6.95 (d, J = 9.0 Hz, 2H, H_{Ar}), 3.01 (t, 1H, J = 24.0 Hz, P_2CH). ^{13}C NMR (75 MHz, D_2O) δ 150.9 (C_{Ar}-OP), 133.6 (t, J = 6.7 Hz, C_{Ar}), 130.5 (CH_{Ar}), 119.2 (CH_{Ar}), 49.4 (t, J_{CP} = 113.3 Hz, CH). ^{31}P NMR (121 MHz, D_2O, 85% H_3PO_4) δ 18.72 (2 P), 0.24 (P). HPLC T_r = 1.38 (97% rel. area). HRMS (ESI-) calcd for $C_7H_8Li_2O_{10}P_3$ $[M - 4Li + 3H]^-$ 358.9651, found 358.9658.

Tetraethyl ((6-Hydroxynaphthalen-2-yl)methylene)bis(phosphonate) 5. Sodium metal (400 mg, 17.42 mmol, 3 equiv) was added in small portions to diethyl phosphite (14 mL, 110.35 mmol, 19 equiv), ensuring that the temperature of the mixture never exceeded 50 °C. 6-Hydroxy-2-naphthaldehyde (1 g, 5.81 mmol, 1 equiv) was added to the solution and the reaction mixture was stirred at rt under argon for 48 h. The reaction was quenched by addition of H_2O (100 mL) and the product was extracted with $CHCl_3$ (3 x 100 mL). The organic layers were combined, washed with brine, dried over anhydrous $MgSO_4$, filtered, and evaporated. The crude material was dissolved in minimum volume of CH_2Cl_2 and precipitated by addition of cyclohexane to yield **5** as a white solid (2.01 g, 80%). Mp 124-126 °C. R_f = 0.60 (silica gel, 95:5 CH_2Cl_2:MeOH). ^{1}H NMR (300 MHz, $CDCl_3$) δ 7.72 (s, 1H, H_{Ar}), 7.40 (m, 2H, H_{Ar}), 7.26-7.23 (m, 1H, H_{Ar}), 6.84 (d, J = 3.0 Hz, 1H, H_{Ar}), 6.80 (s, 1 H, H_{Ar}), 4.24-3.94 (m, 4H + 2H + 2H, diastereotopic POCH_2CH$_3$), 3.85 (t, J = 24.0 Hz, 1H, P$_2$CH), 1.33, 1.16 (two t, J = 6.0 Hz, 6H + 6H, POCH$_2$CH_3). ^{13}C NMR (75 MHz, $CDCl_3$) δ 155.2 (C_{Ar}OH), 134.0 (C_{Ar}), 129.5 (CH$_{Ar}$), 129.1 (CH$_{Ar}$), 128.2 (C_{Ar}), 127.9 (CH$_{Ar}$), 126.8 (CH$_{Ar}$), 123.1 (C_{Ar}), 118.8 (CH$_{Ar}$), 109.1 (CH$_{Ar}$), 63.6, 63.6, 63.3, 63.2 (4 x CH$_2$), 45.2 (t, J_{CP} = 133.5 Hz, CH), 16.4, 16.3, 16.3, 16.2 (4 x CH$_3$). ^{31}P NMR (121 MHz, $CDCl_3$, 85% H_3PO_4) δ 18.87 (2 P). HPLC T_r = 2.92 (91% rel. area). MS (ESI+) $[M + H]^+$ 431.1, $[M + Na]^+$ 453.1, $[2M + Na]^+$ 883.3. HRMS (ESI+) calcd for $C_{19}H_{28}O_7P_2Na$ $[M + Na]^+$ 453.1202, found 453.1198.

6-(Bis(diethoxyphosphoryl)methyl)naphthalen-2-yl Diethyl Phosphate 6. Compound **5** (500 mg, 1.16 mmol, 1.0 equiv) and 1,4-diazabicyclo[2.2.2]octane (DABCO, 392 mg, 3.48 mmol, 3 equiv) were dissolved in anhydrous THF (5 mL) and diethyl chlorophosphate (0.50 mL, 3.48 mmol, 3 equiv) was added dropwise at rt. The mixture was stirred for 48 h at rt under argon and then poured into CH_2Cl_2, washed with saturated NH_4Cl, brine, dried over anhydrous $MgSO_4$, filtered, and evaporated. The crude material was purified by column chromatography (silica gel,

96:4 EtOAc:MeOH) to yield **6** as a clear yellow oil (380 mg, 58%). R_f = 0.66 (silica gel, 95:5 CH_2Cl_2:MeOH). ^{1}H NMR (300 MHz, $CDCl_3$) δ 7.92 (s, 1H, H_{Ar}), 7.78 (dd, J = 9.0 Hz, J = 15.0 Hz, 2H, H_{Ar}), 7.64-7.57 (m, 2H, H_{Ar}), 7.34 (dd, J = 3.0 Hz, J = 9.0 Hz, 1H, H_{Ar}), 4.26-3.86 (m, 13H, 12H x diastereotopic POCH_2CH$_3$; 1H x P$_2$CH), 1.36, 1.26, 1.12 (three t, J = 6.0 Hz, 6H + 6H + 6H, POCH$_2$CH_3). ^{13}C NMR (75 MHz, $CDCl_3$) δ 148.7 (C_{Ar}-OP), 133.2 (C_{Ar}), 130.8 (C_{Ar}), 130.0 (CH$_{Ar}$), 129.4 (CH$_{Ar}$), 129.3 (CH$_{Ar}$), 129.1 (CH$_{Ar}$), 127.9 (C_{Ar}), 120.6 (CH$_{Ar}$), 116.3 (CH$_{Ar}$), 64.9, 64.8, 63.6, 63.1 (6 x CH$_2$), 45.8 (t, J_{CP} = 132.0 Hz, CH), 16.4, 16.3, 16.2 (6 x CH$_3$). ^{31}P NMR (121 MHz, $CDCl_3$, 85% H_3PO_4) δ 18.39 (2 P), -6.26 (P). HPLC T_r = 5.22 (96% rel. area). MS (ESI+) [M + Na]$^+$ 589.1. HRMS (ESI+) calcd for $C_{23}H_{37}O_{10}P_3Na$ [M + Na]$^+$ 589.1492, found 589.1489.

Tetraethyl ((4-Hydroxyphenyl)methylene)bis(phosphonate) 7.[34,35] Sodium metal (566 mg, 24.60 mmol, 3 equiv) was added in small portions to diethyl phosphite (20 mL, 155.80 mmol, 19 equiv), ensuring that the temperature of the mixture never exceeded 50 °C. 4-Hydroxybenzaldehyde (1 g, 8.20 mmol, 1 equiv) was added to the solution and the reaction mixture was stirred at rt under argon for 48 h. After this time, the reaction was quenched by addition of H_2O (100 mL) and the product was extracted with $CHCl_3$ (3 x 100 mL). The organic layers were combined, washed with brine, dried over anhydrous $MgSO_4$, filtered, and evaporated to yield **7** as a white solid (3.12 g, 99%.). ^{1}H and ^{31}P NMR data are in complete agreement with literature data.[34,35] Additional analytical data are provided. Mp 89-90 °C. R_f = 0.55 (silica gel, 95:5 CH_2Cl_2:MeOH). ^{1}H NMR (300 MHz, $CDCl_3$) δ 7.20 (d, J = 9.0 Hz, 2H, ArH), 6.70 (d, J = 9.0 Hz, 2H, ArH), 4.12, 4.00, 3.88 (three m, 4H + 2H + 2H, diastereotopic POCH_2CH$_3$), 3.63 (t, J = 24.0 Hz, 1H, P$_2$CH), 1.29, 1.14 (two t, J = 6.0 Hz, 6H + 6H, POCH$_2$CH_3). ^{13}C NMR (75 MHz, $CDCl_3$) δ 157.2 (C_{Ar}OH), 131.6 (t, J = 6.0 Hz, CH$_{Ar}$), 119.3 (t, J = 7.5 Hz, C_{Ar}), 116.3 (CH$_{Ar}$), 63.8, 63.7, 63.2, 63.2 (4 x CH$_2$), 44.4 (t, J_{CP} = 134.3 Hz, CH), 16.5, 16.4, 16.3, 16.3 (4 x CH$_3$). ^{31}P NMR (121

MHz, $CDCl_3$, 85% H_3PO_4) δ = 19.00 (2 P). HPLC T_r = 2.25 (98% rel. area). MS (ESI+) $[M + H]^+$ 381.1, $[M + Na]^+$ 403.1. HRMS (ESI+) calcd for $C_{15}H_{26}O_7P_2Na$ $[M + Na]^+$ 403.1046, found 403.1050.

Tetraethyl ((4-(Diethylphospho)phenyl)methylene)bis(phosphonate) 8. Compound **7** (650 mg, 1.71 mmol, 1.0 equiv) and 1,4-diazabicyclo[2.2.2]octane (DABCO, 575 mg, 10.26 mmol, 3 equiv) were dissolved in anhydrous THF (5 mL) and diethyl chlorophosphate (0.74 mL, 10.26 mmol, 3 equiv) was added dropwise at rt. The mixture was stirred for 48 h at rt under argon and then poured into CH_2Cl_2, washed with saturated NH_4Cl, brine, dried over anhydrous $MgSO_4$, filtered, and evaporated. The crude material was purified by column chromatography (CH_2Cl_2:MeOH, 96:4) to yield **8** as a clear yellow oil (703 mg, 80%). R_f = 0.63 (silica gel, 95:5 CH_2Cl_2:MeOH). ^{1}H NMR (300 MHz, $CDCl_3$) δ 7.42 (d, J = 9.0 Hz, 2H, *ArH*), 7.17 (d, J = 9.0 Hz, 2H, *ArH*), 4.17, 4.09, 3.95, 3.88 (four m, 12H, diastereotopic POCH_2CH$_3$), 3.68 (t, J = 24.0 Hz, 1H, P$_2$*CH*), 1.30, 1.24, 1.12 (three t, J = 6.0 Hz, 6H + 6H + 6H, POCH$_2$*CH*$_3$). ^{13}C NMR (75 MHz, $CDCl_3$) δ 150.3 (C_{Ar}OP), 131.9 (t, J = 6.0 Hz, CH_{Ar}), 127.0 (C_{Ar}), 120.1 (CH_{Ar}), 64.7, 64.7, 63.6, 63.5, 63.1, 63.0 (6 x CH_2), 44.9 (t, J_{CP} = 132.0 Hz, *C*H), 16.3, 16.2, 16.1 (6 x CH_3). ^{31}P NMR (121 MHz, $CDCl_3$, 85% H_3PO_4) δ 18.29 (2 P), -6.60 (P). HPLC: T_r = 3.52 (96% rel. area). MS (ESI+) $[M + H]^+$ 517.2, $[M + Na]^+$ 539.1. HRMS (ESI+) calcd for $C_{19}H_{35}O_{10}P_3Na$ $[M + Na]^+$ 539.1335, found 539.1333.

Materials. Fru(1,6)P_2, glycerol-3-phosphate dehydrogenase and triose-phosphate isomerase were purchased from Sigma-Aldrich. NADH was from Roche Diagnostics. All other chemicals and materials were obtained from Sigma-Aldrich, Fisher Scientific, Bioshop Canada, and GE Healthcare Life Sciences.

Purification and Crystallization. Expression and purification of recombinant native (WT) rabbit muscle aldolase was performed as described previously[27,69] using *Escherichia coli* strain BL21-SI for overexpression of the recombinant protein (Invitrogen). Enzyme concentration was determined using an extinction coefficient of 0.91 cm mg^{-1} mL at 280 nm.[70] The native enzyme was crystallized by vapor diffusion from a 1:1 mixture of protein solution (10 mg/mL in 20 mM Tris-HCl, pH 7.0) and precipitant buffer (18% polyethylene glycol 4000 in 0.1 M Na-HEPES, pH 7.5) that was equilibrated against a reservoir of precipitant, as described previously.[27]

Crystallographic Data Collection and Processing. Aldolase crystals were soaked for either 30 min or 60 min in crystallization liquor containing one of the following ligands (**1** (NA-P_2), **2** (PNAB), **3** (NAB), or **4** (PBB)) at 1, 5, or 20 mM (final concentration in the mother liquor). Prior to flash-freezing in liquid nitrogen, crystals were cryoprotected by briefly soaking in a mother liquor solution containing 15% (v/v) glycerol and ligand at an appropriate concentration. Data for **1** was collected at beamlines X25 and X29 of the National Synchrotron Light Source at Brookhaven National Laboratories. The remaining datasets were collected from single crystals at beamline 08ID-1 or 08B1-1 of the Canadian Light Source, Saskatchewan, Canada. A native data set was also collected as a control. All data sets were processed with HKL2000,[71] and the data reduction results are shown in Table 4.

Table 4. Data Collection and Refinement Statistics

Structure	ALDOA-**1**	ALDOA-**2**	ALDOA-**3**	ALDOA-**4**
Data Collection				
PDB code	5TLZ	5TLE	5TLH	5TLW
Resolution range (Å)	44.04 - 1.97	32.34 - 1.58	43.74 - 2.20	43.66 - 2.29
Space group	P 2_1	P 2_1	P 2_1	P 2_1
Unit cell a (Å), b (Å), c (Å), β (°)	83.3 103.6 84.5 98.7	83.7 103.7 84.5 98.8	83.6 103.1 84.9 98.9	83.9 102.7 84.9 98.5
Wavelength (Å)	1.1	0.9795	0.9795	0.9795
Total / Unique reflections	277501 / 86719	541509/185199	332045 / 69202	192056 / 59193
Multiplicity	3.2	2.9 (2.4)	4.8 (4.4)	3.2 (2.6)
Completeness (%)	0.87	0.94 (0.97)	0.96 (0.92)	0.88 (0.44)
Average $I/\sigma(I)$	20.07	13.96 (1.46)	6.50 (2.88)	5.87 (1.78)
Wilson B-factor	21.83	18.22	24.98	28.71
R_{merge} [b]	0.052	0.03856 (0.71)	0.1792 (1.175)	0.1541 (0.9413)
R_{meas} [c]	-	0.0465 (0.8927)	0.1996 (1.321)	0.1823 (1.175)
CC1/2	-	0.999 (0.575)	0.986 (0.684)	0.982 (0.485)
Refinement				
R_{work} (%) [d]	0.1287 (0.2041)	0.1314 (0.2630)	0.1504 (0.2169)	0.1521 (0.2236)
R_{free} (%) [e]	0.1665 (0.2705)	0.1576 (0.2862)	0.1880 (0.2606)	0.1922 (0.2918)
Number of atoms	12322	13159	11644	11402
macromolecules	10644	10801	10662	10654
ligands	184	120	140	104
RMSD (bond length) (Å)	0.006	0.008	0.005	0.004
RMSD (angles) (°)	0.76	0.92	0.86	0.63
Ramachandran favored (%)	98	98	98	97
Ramachandran allowed (%)	2	2	2.1	2.5
Average B-factor (Å^2)	29.13	26.99	32.02	37.80

[a] All values in parentheses are given for the highest resolution shell; [b] $R_{merge} = \sum_{hkl}\sum_i \left| I_i(hkl) - \bar{I}_i(hkl) \right| / \sum_{hkl}\sum_i I_i(hkl)$, with i running over the number of independent observations of reflection hkl; [c] $R_{meas} = \sum_{hkl}(n/(n-1))^{1/2}\sum_{i=1}^{n} \left| I_i(hkl) - \bar{I}_i(hkl) \right| / \sum_{hkl}\sum_i I_i(hkl)$; [d] $R_{work} = \sum_{hkl} \left\| I_o(hkl) \right| - \left| I_c(hkl) \right\| / \sum_{hkl} \left| I_o(hkl) \right|$; [e] $R_{free} = \sum_{hkl \epsilon T} \left\| I_o(hkl) \right| - \left| I_c(hkl) \right\| / \sum_{hkl \epsilon T} \left| I_o(hkl) \right|$, where T is a test data set randomly selected from the observed reflections prior to refinement. Test data set was not used throughout refinement and contains a minimum of 2000 unique reflections (or 5%) (the smaller value is selected).

Structure determination and refinement. Crystal structures were determined by molecular replacement with PHENIX[72] Phaser-MR[73] using the native aldolase homotetramer structure as a reference model [Protein Data Bank (PDB) entry 1ZAH]. Refinement and model building were performed with phenix.refine[74] and Coot[75] respectively. Data quality and resolution cut-off was assessed using correlation-coefficient-based criteria, CC1/2.[76] Ligand fitting and interpretation was performed by a combination of simulated annealing $F_o - F_c$ omit maps and feature-enhanced sigma-A weighted $2F_o - F_c$ maps[77] that were calculated in the final round of refinement. All difference density maps ($F_o - F_c$) shown in the paper correspond to simulated annealed $F_o - F_c$ omit maps. Ligand coordinate and restraints were generated using PHENIX eLBOW.[78] Final model statistics were calculated with MolProbity[79] and are shown in Table 4. The coordinates and structure factors of the crystallographic structures have been deposited in the Protein Data Bank (PDB entries: 5TLE, 5TLH, 5TLW, 5TLZ). All figures were prepared using PyMOL (http://www.pymol.org).[80]

Structures requiring modeling of multiple conformations of ligand in the active site were prepared by the following sequence: occupancies of the multiple conformations were determined using a triplicate convergence test performed by setting arbitrary initial occupancies to three different values and averaging the refined occupancies.

In order to calculate electrostatic surface potentials, the Adaptive Poisson-Boltzmann Solver (APBS) software package was used.[81,82] The structure was prepared for APBS with the automated pipeline provided by PDB2PQR,[83,84] which adds any missing hydrogens, determines side-chain p*K*as, and assigns force field parameters for atom charge and radius (PARSE force filed was selected by default).

Activity assays. Aldolase cleavage activity was determined using a coupled assay system involving triose-phosphate isomerase and glycerol-3-phosphate dehydrogenase (TIM/GDH) by following NADH oxidation at 340 nm using a Varian Cary 300 UV-Vis spectrophotometer thermostated at 25 °C.[85] Activity was measured by the addition of aldolase to a solution containing substrate (FBP) made up in assay buffer (50 mM Tris-Acetate, pH 7.5, 1 mM EDTA, 0.3 mM NADH, and containing coupling enzymes (5 μg/mL GDH and 0.5 μg/mL TIM) to a final volume of 1 mL). All kinetic values reported comprise a minimum of three independent assays, including the inhibition studies. The raw kinetic data is freely available upon request from the authors.

Kinetic methods: (A) IC50 determinations. IC50s for aldolase inhibition by **2** were measured in activity assay conditions described above with concentrations of **2** ranging from 0.01 μM – 20 μM and a substrate (FBP) concentration of 10 μM. Aldolase was pre-incubated for 0 – 180 min with **2** prior to activity determination. IC50s were calculated using full 4 parameter IC50 model in GraFit Data Analysis Software.[86] For all calculations, the y-range was 5 – 6 U/mg, slope factors were ~1.5, and Chi^2 ~1.5 – 3.

Kinetic methods: (B) Slow-binding Inhibition. Slow-binding inhibition was analyzed according to Scheme 2 assuming rapid formation of an enzyme inhibitor complex (EI) that can undergo slow rotational isomerization to a second enzyme inhibitor complex (EI*).[45,87] All rate steps are assumed to be fast relative to k_{+4} and k_{-4}. For this kinetic sequence, K_i* represents the overall inhibition constant, and K_i the dissociation constant for the Michaelis complex EI.

Scheme 2. General mechanism for describing slow-binding inhibition.

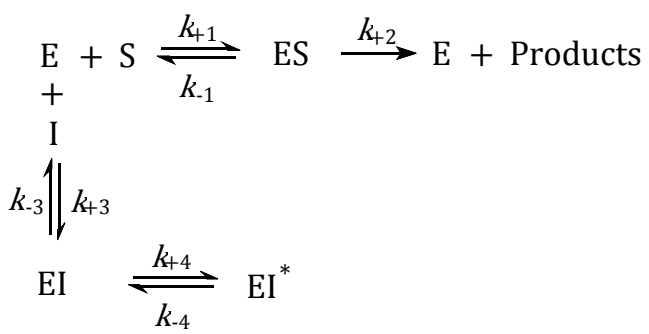

$$K_{\mathrm{m}} = \frac{V_M[S]}{K_M + [S]} \qquad K_{\mathrm{i}} = \frac{k_{-3}}{k_{+3}} \qquad K_{\mathrm{i}}^{*} = K_{\mathrm{i}} \frac{k_{-4}}{(k_{+4} + k_{-4})}$$

The slow-binding inhibition constants for inhibitor **2** were determined by non-linear regression analysis of progress curves measured in the presence of 20 – 200 μM FBP and 0.5 – 75 μM of **2**. Slow-binding inhibitors are characterized by an initial burst of reaction followed by a slower steady state where progressive curves exhibit asymptotic behavior. All progressive curves were analyzed according to eq. 1, which was fitted using GraFit Data Analysis Software v.6.0.12 yielding kinetic parameters v_o, v_s, and k_a, described by eq. 2 – 4 below. Linearized Dixon plots derived from these parameters were then used to determine K_{m}, K_{i} as well as k_{+4} and k_{-4}.

$$[P]_t = v_s t + \frac{(v_o - v_s)(1 - e^{-k_a t})}{k_a} + C \qquad (1)$$

$$v_O = \frac{V_m[S]}{K_m\left(1 + \frac{[I]}{K_i}\right) + [S]} \qquad (2)$$

$$v_S = \frac{V_m[S]}{K_m\left(1 + \frac{[I]}{K_i{}^*}\right) + [S]} \qquad (3)$$

$$k_a = k_{-4} + \frac{k_{+4}[I]}{K_i\left(1 + \frac{[S]}{K_m}\right) + [I]} \qquad (4)$$

Kinetic methods: (C) Competitive Inhibition. The inhibition constant (K_{i}) for compound **4** were determined from double-reciprocal plots of initial rates measured in the presence of 5 – 200 μM FBP and 10 - 200 μM inhibitor at constant enzyme concentration (0.01 μg/mL).

Kinetic methods: (D) Dual Competitive Inhibition. For compound **3**, inhibition kinetics were analyzed using a dual reversible linear inhibition model described previously.[46] The following equation used in the GraFit Data Analysis Software v.6.0.12 to analyze the inhibition data:

$$v = \frac{V_{max}[S]}{K_m\left(1 + \frac{[I]}{K_i} + \frac{[I]}{K_i'} + \frac{[I][I]}{K_i K_i'}\right)} \quad (5)$$

where K_i and K_i' represent the inhibition constants for the two competitive binding sites. Assay conditions were the same as described for competitive inhibition.

Cellular growth inhibition tests. HeLa cells and HEK293 were selected for the *in vivo* growth inhibition assays. Cells were seeded into 6-well plates at densities of 2 x 10^5 cells/plate (HEK293) and 3 x 10^5 cells/plate (HeLa) (final volume 2 mL). Cells were cultured using DMEM and maintained at 37 ^oC/ 5% CO_2 for 24, 48 or 72 h. Treated cells received a final dose of 0.1, 1.0 or 10 µM of filter-sterilized **2**. Cells were harvested by first washing cells with pre-warmed PBS and detached using trypsin (0.5 mL x (0.05% trypsin for HEK293 and 0.25% for HELA cells)). Trypsin was diluted by addition of 1.5 mL growth medium (DMEM). Cells were transferred to 15-mL conical tubes and centrifuged at 200 x g for 5 min. Cells were resuspended in 0.5 mL of pre-warmed growth medium. A 1:1 mixture of the cell suspension was mixed with Trypan Blue exclusion solution for subsequent total cell counting with a hemocytometer. The average number of cells was the result of counting three replicates in two independent experiments.

ASSOCIATED CONTENT

Supporting Information

The Supporting Information is available free of charge on the ACS Publications website at DOI: xxxx.

- Active site comparisons of aldolase A in complex with **1-2** and FBP, comparison of aldolase A binding with **3** and NASEP, inhibition kinetics for **2-4**, HPLC assessment and ^{1}H and ^{13}C NMR spectra of **2-4** (PDF)
- PDB ID Codes: 5TLZ (ALDOA-**1**), 5TLE (ALDOA-**2**), 5TLH (ALDOA-**3**), 5TLW (ALDOA-**4**). Atomic coordinates and experimental data are accessible on the Protein Data Bank.
- Molecular strings formula for **1-4** as well as respective K_i against aldolase A and mode of inhibition (CSV)

AUTHOR INFORMATION

Corresponding Author

*Jurgen Sygusch. E-mail: jurgen.sygusch@umontreal.ca; Tel.: 514-343-2389; Fax: 514-343-6463.

†Laurent Salmon. E-mail: laurent.salmon@u-psud.fr; Tel: 33 1 69 15 63 11; Fax: 33 1 69 15 72 81.

Author Contributions

†MAF and LS synthesized the compounds used in this study. *PH collected and solved the crystal structures; produced all kinetic data; and wrote the manuscript. *Conception and design of the project and critical manuscript revisions were provided by JS. All authors have given approval to the final version of the manuscript.

Funding Sources

This work was supported by funding from the National Science and Engineering Research Council of Canada (NSERC- RGPIN-2016-04898) to JS. PH is the recipient of a Ph.D. scholarship from the NSERC – Collaborative Research and Training Experience Program (CREATE). MAF and LS are members of the Laboratory of Excellence in Research on Medication and Innovative Therapeutics (LERMIT) supported by a grant from ANR (ANR-10-LABX-33) and of the Joint Programming Initiative on AntiMicrobial Resistance (JPIAMR) supported by a grant from ANR (DesInMBL).

Notes

The authors declare no competing financial interests.

ACKNOWLEDGMENTS

We wish to thank Miguel St-Jean for collecting the crystallographic data for the aldolase – **1** complex. We also wish to thank Rachid Djillali and Casimir Blonski for their valuable contributions and discussions regarding the synthesis of compounds **1** to **4**. J.-P. Baltaze, T. Inceoglu, and E. Rascol are gratefully acknowledged for technical assistance in NMR, MS, and HPLC analyses. Diffraction data for aldolase in complex with compound **1** on beamlines X25 and X29 of the National Synchrotron Light Source. Financial support comes principally from the Offices of Biological and Environmental Research and of Basic Energy Sciences of the US Department of Energy (Contract No. DE-AC02-98CH10886), and from the National Center for Research Resources (P41RR012408) and the National Institutes of Health (P41GM103473). Kind assistance by beamline personnel, Drs L. Flaks, A. Héroux and H. Robinson, is gratefully acknowledged.

Diffraction data for aldolase in complex with compounds **2**, **3**, and **4** was collected on beamlines 08ID-1 and 08B1-1 at the Canadian Light Source, which is supported by the Natural Sciences and Engineering Research Council of Canada, the National Research Council Canada, the Canadian Institutes of Health Research, the Province of Saskatchewan, Western Economic Diversification Canada, and the University of Saskatchewan. Data was collected with the assistance of Shaun Labiuk.

We also wish to thank Louise Cournoyer for her kind assistance in conducting the cellular assays.

ABBREVIATIONS USED

FBP, Fructose-1,6-bisphosphate; NA-P_2, naphthalene 2,6-bisphosphate; ALDOA, aldolase A; PDB, Protein Data Bank.

REFERENCES

(1) Som, P.; Atkins, H. L.; Bandoypadhyay, D.; Fowler, J. S.; MacGregor, R. R.; Matsui, K.; Oster, Z. H.; Sacker, D. F.; Shiue, C. Y.; Turner, H.; Wan, C.-N.; Wolf, A. P.; Zabinski, S. V. A Fluorinated Glucose Analog, 2-Fluoro-2-Deoxy-D-Glucose (F-18): Nontoxic Tracer for Rapid Tumor Detection. *J. Nucl. Med.* **1980**, *21* (7), 670–675.

(2) Warburg, O.; Wind, F.; Negelein, E. The Metabolism of Tumors in the Body. *J. Gen. Physiol.* **1927**, *8* (6), 519–530.

(3) Lunt, S. Y.; Heiden, M. G. V. Aerobic Glycolysis: Meeting the Metabolic Requirements of Cell Proliferation. *Annu. Rev. Cell Dev. Biol.* **2011**, *27* (1), 441–464.

(4) Cairns, R. A.; Harris, I. S.; Mak, T. W. Regulation of Cancer Cell Metabolism. *Nat. Rev. Cancer* **2011**, *11* (2), 85–95.

(5) Ganapathy-Kanniappan, S.; Geschwind, J.-F. H. Tumor Glycolysis as a Target for Cancer Therapy: Progress and Prospects. *Mol. Cancer* **2013**, *12* (1), 152.

(6) Rho, J.-H.; Roehrl, M. H. A.; Wang, J. Y. Glycoproteomic Analysis of Human Lung Adenocarcinomas Using Glycoarrays and Tandem Mass Spectrometry: Differential Expression and Glycosylation Patterns of Vimentin and Fetuin A Isoforms. *Protein J.* **2009**, *28* (3–4), 148–160.

(7) Poschmann, G.; Sitek, B.; Sipos, B.; Ulrich, A.; Wiese, S.; Stephan, C.; Warscheid, B.; Klöppel, G.; Vander Borght, A.; Ramaekers, F. C. S.; Meyer, H. E.; Stühler, K. Identification of Proteomic Differences between Squamous Cell Carcinoma of the Lung and Bronchial Epithelium. *Mol. Cell. Proteomics MCP* **2009**, *8* (5), 1105–1116.

(8) Du, S.; Guan, Z.; Hao, L.; Song, Y.; Wang, L.; Gong, L.; Liu, L.; Qi, X.; Hou, Z.; Shao, S. Fructose-Bisphosphate Aldolase A Is a Potential Metastasis-Associated Marker of Lung

Squamous Cell Carcinoma and Promotes Lung Cell Tumorigenesis and Migration. *PLoS ONE* **2014**, *9* (1), e85804.

(9) Pfleiderer, G.; Thöner, M.; Wachsmuth, E. D. Histological Examination of the Aldolase Monomer Composition of Cells from Human Kidney and Hypernephroid Carcinoma. *Beitr. Pathol.* **1975**, *156* (3), 266–279.

(10) Chaerkady, R.; Harsha, H. C.; Nalli, A.; Gucek, M.; Vivekanandan, P.; Akhtar, J.; Cole, R. N.; Simmers, J.; Schulick, R. D.; Singh, S.; Torbenson, M.; Pandey, A.; Thuluvath, P. J. A Quantitative Proteomic Approach for Identification of Potential Biomarkers in Hepatocellular Carcinoma. *J. Proteome Res.* **2008**, *7* (10), 4289–4298.

(11) Ji, S.; Zhang, B.; Liu, J.; Qin, Y.; Liang, C.; Shi, S.; Jin, K.; Liang, D.; Xu, W.; Xu, H.; Wang, W.; Wu, C.; Liu, L.; Liu, C.; Xu, J.; Ni, Q.; Yu, X. ALDOA Functions as an Oncogene in the Highly Metastatic Pancreatic Cancer. *Cancer Lett.* **2016**, *374* (1), 127–135.

(12) Peng, Y.; Li, X.; Wu, M.; Yang, J.; Liu, M.; Zhang, W.; Xiang, B.; Wang, X.; Li, X.; Li, G.; Shen, S. New Prognosis Biomarkers Identified by Dynamic Proteomic Analysis of Colorectal Cancer. *Mol. Biosyst.* **2012**, *8* (11), 3077–3088.

(13) Opperdoes, F. R. Compartmentation of Carbohydrate Metabolism in Trypanosomes. *Annu. Rev. Microbiol.* **1987**, *41* (1), 127–151.

(14) Verlinde, C. L. M. J.; Hannaert, V.; Blonski, C.; Willson, M.; Périé, J. J.; Fothergill-Gilmore, L. A.; Opperdoes, F. R.; Gelb, M. H.; Hol, W. G. J.; Michels, P. A. M. Glycolysis as a Target for the Design of New Anti-Trypanosome Drugs. *Drug Resist. Updat.* **2001**, *4* (1), 50–65.

(15) Dax, C.; Duffieux, F.; Chabot, N.; Coincon, M.; Sygusch, J.; Michels, P. A. M.; Blonski, C. Selective Irreversible Inhibition of Fructose 1,6-Bisphosphate Aldolase from Trypanosoma Brucei. *J. Med. Chem.* **2006**, *49* (5), 1499–1502.

(16) Suh, B.; Barker, R. Fluorescence Studies of the Binding of Alkyl and Aryl Phosphates to Rat Muscle Aldolase. *J. Biol. Chem.* **1971**, *246* (22), 7041–7050.

(17) Blonski, C.; De Moissac, D.; Périé, J.; Sygusch, J. Inhibition of Rabbit Muscle Aldolase by Phosphorylated Aromatic Compounds. *Biochem. J.* **1997**, *323* (Pt 1), 71–77.

(18) Dax, C.; Coinçon, M.; Sygusch, J.; Blonski, C. Hydroxynaphthaldehyde Phosphate Derivatives as Potent Covalent Schiff Base Inhibitors of Fructose-1,6-Bisphosphate Aldolase †. *Biochemistry (Mosc.)* **2005**, *44* (14), 5430–5443.

(19) Tauro, M.; Loiodice, F.; Ceruso, M.; Supuran, C. T.; Tortorella, P. Arylamino Bisphosphonates: Potent and Selective Inhibitors of the Tumor-Associated Carbonic Anhydrase XII. *Bioorg. Med. Chem. Lett.* **2014**, *24* (8), 1941–1943.

(20) Savino, S.; Toscano, A.; Purgatorio, R.; Profilo, E.; Laghezza, A.; Tortorella, P.; Angelelli, M.; Cellamare, S.; Scala, R.; Tricarico, D.; Marobbio, C. M.; Perna, F.; Vitale, P.; Agamennone, M.; Dimiccoli, V.; Tolomeo, A.; Scilimati, A. Novel Bisphosphonates with Antiresorptive Effect in Bone Mineralization and Osteoclastogenesis. *Eur. J. Med. Chem.* **2018**, *158*, 184–200.

(21) Montalvetti, A.; Bailey, B. N.; Martin, M. B.; Severin, G. W.; Oldfield, E.; Docampo, R. Bisphosphonates Are Potent Inhibitors of Trypanosoma Cruzi Farnesyl Pyrophosphate Synthase. *J. Biol. Chem.* **2001**, *276* (36), 33930–33937.

(22) Dhar, M. K.; Koul, A.; Kaul, S. Farnesyl Pyrophosphate Synthase: A Key Enzyme in Isoprenoid Biosynthetic Pathway and Potential Molecular Target for Drug Development. *New Biotechnol.* **2013**, *30* (2), 114–123.

(23) Wills, V. S.; Metzger, J. I.; Allen, C.; Varney, M. L.; Wiemer, D. F.; Holstein, S. A. Bishomoisoprenoid Triazole Bisphosphonates as Inhibitors of Geranylgeranyl Diphosphate Synthase. *Bioorg. Med. Chem.* **2017**, *25* (8), 2437–2444.

(24) K-M Chen, C.; Hudock, M. P.; Zhang, Y.; Guo, R.-T.; Cao, R.; No, J. H.; Liang, P.-H.; Ko, T.-P.; Chang, T.-H.; Chang, S.-C.; Song, Y.; Axelson, J.; Kumar, A.; Wang, A. H.-J.; Oldfield, E. Inhibition of Geranylgeranyl Diphosphate Synthase by Bisphosphonates: A Crystallographic and Computational Investigation. *J. Med. Chem.* **2008**, *51* (18), 5594–5607.

(25) Yanvarev, D. V.; Korovina, A. N.; Usanov, N. N.; Khomich, O. A.; Vepsäläinen, J.; Puljula, E.; Kukhanova, M. K.; Kochetkov, S. N. Methylene Bisphosphonates as the Inhibitors of HIV RT Phosphorolytic Activity. *Biochimie* **2016**, *127*, 153–162.

(26) Freemont, P. S.; Dunbar, B.; Fothergill-Gilmore, L. A. The Complete Amino Acid Sequence of Human Skeletal-Muscle Fructose-Bisphosphate Aldolase. *Biochem. J.* **1988**, *249* (3), 779–788.

(27) St-Jean, M.; Lafrance-Vanasse, J.; Liotard, B.; Sygusch, J. High Resolution Reaction Intermediates of Rabbit Muscle Fructose-1,6-Bisphosphate Aldolase: Substrate Cleavage and Induced Fit. *J. Biol. Chem.* **2005**, *280* (29), 27262–27270.

(28) Anai, M.; Lai, C. Y.; Horecker, B. L. The Pyridoxal Phosphate-Binding Site of Rabbit Muscle Aldolase. *Arch. Biochem. Biophys.* **1973**, *156* (2), 712–719.

(29) St-Jean, M.; Blonski, C.; Sygusch, J. Charge Stabilization and Entropy Reduction of Central Lysine Residues in Fructose-Bisphosphate Aldolase. *Biochemistry (Mosc.)* **2009**, *48* (21), 4528–4537.

(30) St-Jean, M.; Sygusch, J. Stereospecific Proton Transfer by a Mobile Catalyst in Mammalian Fructose-1,6-Bisphosphate Aldolase. *J. Biol. Chem.* **2007**, *282* (42), 31028–31037.

(31) Ramaswamy, B.; Shapiro, C. L. Bisphosphonates in the Prevention and Treatment of Bone Metastases. *Oncol. Williston Park N* **2003**, *17* (9), 1261-1270; discussion 1270-1272, 1277–1278, 1280.

(32) Reid, I. R. Short-Term and Long-Term Effects of Osteoporosis Therapies. *Nat. Rev. Endocrinol.* **2015**, *11* (7), 418–428.

(33) Tauro, M.; Loiodice, F.; Ceruso, M.; Supuran, C. T.; Tortorella, P. Dual Carbonic Anhydrase/Matrix Metalloproteinase Inhibitors Incorporating Bisphosphonic Acid Moieties Targeting Bone Tumors. *Bioorg. Med. Chem. Lett.* **2014**, *24* (12), 2617–2620.

(34) Vovk, A. I.; Kalchenko, V. I.; Cherenok, S. A.; Kukhar, V. P.; Muzychka, O. V.; Lozynsky, M. O. Calix[4]arene Methylenebisphosphonic Acids as Calf Intestine Alkaline Phosphatase Inhibitors. *Org. Biomol. Chem.* **2004**, *2* (21), 3162–3166.

(35) Xu, T.; Zhang, L.; Cheng, Z.; Zhu, X. A Novel Methacrylate with a Bisphosphonate Group: RAFT Polymerization and Flame Retardant Property of the Resultant Polymers. *Polym. Chem.* **2015**, *6* (12), 2283–2289.

(36) Pisarek, S.; Bednarski, H.; Gryko, D. An Efficient Method for Phosphorylation of Alcohols: Preparation of Por-phyrin-Derived Phosphates. *Synlett* **2012**, *23* (18), 2667–2671.

(37) Matthiesen, R. A.; Wills, V. S.; Metzger, J. I.; Holstein, S. A.; Wiemer, D. F. Stereoselective Synthesis of Homoneryl and Homogeranyl Triazole Bisphosphonates. *J. Org. Chem.* **2016**, *81* (19), 9438–9442.

(38) Ginsburg, A.; Mehler, A. H. Specific Anion Binding to Fructose Diphosphate Aldolase from Rabbit Muscle. *Biochemistry (Mosc.)* **1966**, *5* (8), 2623–2634.

(39) Williams, D. H.; Searle, M. S.; Mackay, J. P.; Gerhard, U.; Maplestone, R. A. Toward an Estimation of Binding Constants in Aqueous Solution: Studies of Associations of Vancomycin Group Antibiotics. *Proc. Natl. Acad. Sci.* **1993**, *90* (4), 1172–1178.

(40) Gallivan, J. P.; Dougherty, D. A. A Computational Study of Cation−π Interactions vs Salt Bridges in Aqueous Media: Implications for Protein Engineering. *J. Am. Chem. Soc.* **2000**, *122* (5), 870–874.

(41) Dougherty, D. A. Cation-π Interactions Involving Aromatic Amino Acids. *J. Nutr.* **2007**, *137* (6), 1504S–1508S.

(42) Gallivan, J. P.; Dougherty, D. A. Cation-π Interactions in Structural Biology. *Proc. Natl. Acad. Sci.* **1999**, *96* (17), 9459–9464.

(43) St-Jean, M.; Izard, T.; Sygusch, J. A Hydrophobic Pocket in the Active Site of Glycolytic Aldolase Mediates Interactions with Wiskott-Aldrich Syndrome Protein. *J. Biol. Chem.* **2007**, *282* (19), 14309–14315.

(44) Rangarajan, E. S.; Park, H.; Fortin, E.; Sygusch, J.; Izard, T. Mechanism of Aldolase Control of Sorting Nexin 9 Function in Endocytosis. *J. Biol. Chem.* **2010**, *285* (16), 11983–11990.

(45) Morrison, J. F.; Walsh, C. T. The Behavior and Significance of Slow-Binding Enzyme Inhibitors. In *Advances in Enzymology and Related Areas of Molecular Biology*; Meister, A., Ed.; John Wiley & Sons, Inc.: New York, 1988; pp 201–301.

(46) Martinez-Irujo, J. J.; Villahermosa, M. L.; Mercapide, J.; Capodevilla, J. F.; Santiago, E. Analysis of the Combined Effect of Two Linear Inhibitors on a Single Enzyme. *Biochem. J.* **1998**, *329* (3), 689–698.

(47) Nicholls, R. A.; Fischer, M.; McNicholas, S.; Murshudov, G. N. Conformation-Independent Structural Comparison of Macromolecules with ProSMART. *Acta Crystallogr. D Biol. Crystallogr.* **2014**, *70* (Pt 9), 2487–2499.

(48) David, P.; Nguyen, H.; Barbier, A.; Baron, R. The Bisphosphonate Tiludronate Is a Potent Inhibitor of the Osteoclast Vacuolar H+-ATPase. *J. Bone Miner. Res.* **1996**, *11* (10), 1498–1507.

(49) Sanofi Winthrop, Inc. Statistical Review and Evaluation of Skelide (Tiludronate Disodium). FDA, Center for drug evaluation and research 1996.

(50) Hartman, F. C.; Barker, R. An Exploration of the Active Site of Aldolase Using Structural Analogs of Fructose Diphosphate*. *Biochemistry (Mosc.)* **1965**, *4* (6), 1068–1075.

(51) Ogata, H.; Takeo, K.; Kuwahara, A.; Suzuno, R.; Fujimoto, M.; Shimizu, J. An Exploration of the Binding Site of Aldolase Using Alkanediol Monoglycolate Bisphosphoric Esters. *Biochim. Biophys. Acta* **1983**, *742* (2), 384–390.

(52) Elliott, T. S.; Slowey, A.; Ye, Y.; Conway, S. J. The Use of Phosphate Bioisosteres in Medicinal Chemistry and Chemical Biology. *MedChemComm* **2012**, *3* (7), 735–751.

(53) Planas, M. E.; Sánchez, S.; González, P.; Rodrigues de Oliveira, J.; Bartrons, R. Protective Effect of Fructose 1,6-Bisphosphate against Carrageenan-Induced Inflammation. *Eur. J. Pharmacol.* **1993**, *237* (2–3), 251–255.

(54) Veras, F. P.; Peres, R. S.; Saraiva, A. L. L.; Pinto, L. G.; Louzada-Junior, P.; Cunha, T. M.; Paschoal, J. A. R.; Cunha, F. Q.; Alves-Filho, J. C. Fructose 1,6-Bisphosphate, a High-

Energy Intermediate of Glycolysis, Attenuates Experimental Arthritis by Activating Anti-Inflammatory Adenosinergic Pathway. *Sci. Rep.* **2015**, *5*, 15171.

(55) Ehringer, W. D.; Niu, W.; Chiang, B.; Wang, O.-L.; Gordon, L.; Chien, S. Membrane Permeability of Fructose-1,6-Diphosphate in Lipid Vesicles and Endothelial Cells. *Mol. Cell. Biochem.* **2000**, *210* (1–2), 35–45.

(56) Grandjean, G.; Jong, P. R. de; James, B. P.; Koh, M. Y.; Lemos, R.; Kingston, J.; Aleshin, A.; Bankston, L. A.; Miller, C. P.; Cho, E. J.; Edupuganti, R.; Devkota, A.; Stancu, G.; Liddington, R. C.; Dalby, K. N.; Powis, G. Definition of a Novel Feed-Forward Mechanism for Glycolysis-HIF1α Signaling in Hypoxic Tumors Highlights Aldolase A as a Therapeutic Target. *Cancer Res.* **2016**, *76* (14), 4259–4269.

(57) Braun, M.; Qorraj, M.; Büttner, M.; Klein, F. A.; Saul, D.; Aigner, M.; Huber, W.; Mackensen, A.; Jitschin, R.; Mougiakakos, D. CXCL12 Promotes Glycolytic Reprogramming in Acute Myeloid Leukemia Cells via the CXCR4/mTOR Axis. *Leukemia* **2016**, *30* (8), 1788–1792.

(58) Caplan, N. A.; Pogson, C. I.; Hayes, D. J.; Blackburn, G. M. Novel Bisphosphonate Inhibitors of Phosphoglycerate Kinase. *Bioorg. Med. Chem. Lett.* **1998**, *8* (5), 515–520.

(59) Kim, C. U.; Luh, B. Y.; Misco, P. F.; Bronson, J. J.; Hitchcock, M. J. M.; Ghazzouli, I.; Martin, J. C. Acyclic Purine Phosphonate Analogs as Antiviral Agents. Synthesis and Structure-Activity Relationships. *J. Med. Chem.* **1990**, *33* (4), 1207–1213.

(60) Périgaud, C.; Gosselin, G.; Lefebvre, I.; Girardet, J.-L.; Benzaria, S.; Barber, I.; Imbach, J.-L. Rational Design for Cytosolic Delivery of Nucleoside Monphosphates : "SATE" and "DTE" as Enzyme-Labile Transient Phosphate Protecting Groups. *Bioorg. Med. Chem. Lett.* **1993**, *3* (12), 2521–2526.

(61) Farquhar, D.; Khan, S.; Srivastva, D. N.; Saunders, P. P. Synthesis and Antitumor Evaluation of Bis[(pivaloyloxy)methyl] 2'-deoxy-5-Fluorouridine 5'-monophosphate (FdUMP): A Strategy to Introduce Nucleotides into Cells. *J. Med. Chem.* **1994**, *37* (23), 3902–3909.

(62) Schultz, C. Prodrugs of Biologically Active Phosphate Esters. *Bioorg. Med. Chem.* **2003**, *11* (6), 885–898.

(63) Mentel, M.; Laketa, V.; Subramanian, D.; Gillandt, H.; Schultz, C. Photoactivatable and Cell-Membrane-Permeable Phosphatidylinositol 3,4,5-Trisphosphate. *Angew. Chem. Int. Ed.* **2011**, *50* (16), 3811–3814.

(64) Subramanian, D.; Laketa, V.; Müller, R.; Tischer, C.; Zarbakhsh, S.; Pepperkok, R.; Schultz, C. Activation of Membrane-Permeant Caged PtdIns(3)P Induces Endosomal Fusion in Cells. *Nat. Chem. Biol.* **2010**, *6* (5), 324–326.

(65) Conway, S. J.; Thuring, J. W.; Andreu, S.; Kvinlaug, B. T.; Roderick, H. L.; Bootman, M. D.; Holmes, A. B. The Synthesis of Membrane Permeant Derivatives of Myo-Inositol 1,4,5-Trisphosphate. *Aust. J. Chem.* **2006**, *59* (12), 887–893.

(66) Li, W.; Schultz, C.; Llopis, J.; Tsien, R. Y. Membrane-Permeant Esters of Inositol Polyphosphates, Chemical Syntheses and Biological Applications. *Tetrahedron* **1997**, *53* (35), 12017–12040.

(67) Atack, J. R.; Cook, S. M.; Watt, A. P.; Fletcher, S. R.; Ragan, C. I. In Vitro and In Vivo Inhibition of Inositol Monophosphatase by the Bisphosphonate L-690,330. *J. Neurochem.* **1993**, *60* (2), 652–658.

(68) Atack, J. R.; Prior, A. M.; Fletcher, S. R.; Quirk, K.; McKernan, R.; Ragan, C. I. Effects of L-690,488, a Prodrug of the Bisphosphonate Inositol Monophosphatase Inhibitor L-

690,330, on Phosphatidylinositol Cycle Markers. *J. Pharmacol. Exp. Ther.* **1994**, *270* (1), 70–76.

(69) Morris, A. J.; Tolan, D. R. Site-Directed Mutagenesis Identifies Aspartate 33 as a Previously Unidentified Critical Residue in the Catalytic Mechanism of Rabbit Aldolase A. *J. Biol. Chem.* **1993**, *268* (2), 1095–1100.

(70) Baranowski, T.; Niederland, T. R. Aldolase Activity of Myogen A. *J. Biol. Chem.* **1949**, *180* (2), 543–551.

(71) Otwinowski, Z.; Minor, W. [20] Processing of X-Ray Diffraction Data Collected in Oscillation Mode. In *Methods in Enzymology*; Charles W. Carter, J., Ed.; Macromolecular Crystallography Part A; Academic Press: New York, 1997; Vol. 276, pp 307–326.

(72) Adams, P. D.; Grosse-Kunstleve, R. W.; Hung, L.-W.; Ioerger, T. R.; McCoy, A. J.; Moriarty, N. W.; Read, R. J.; Sacchettini, J. C.; Sauter, N. K.; Terwilliger, T. C. *PHENIX* : Building New Software for Automated Crystallographic Structure Determination. *Acta Crystallogr. D Biol. Crystallogr.* **2002**, *58* (11), 1948–1954.

(73) McCoy, A. J.; Grosse-Kunstleve, R. W.; Adams, P. D.; Winn, M. D.; Storoni, L. C.; Read, R. J. *Phaser* Crystallographic Software. *J. Appl. Crystallogr.* **2007**, *40* (4), 658–674.

(74) Afonine, P. V.; Grosse-Kunstleve, R. W.; Echols, N.; Headd, J. J.; Moriarty, N. W.; Mustyakimov, M.; Terwilliger, T. C.; Urzhumtsev, A.; Zwart, P. H.; Adams, P. D. Towards Automated Crystallographic Structure Refinement with <phenix.refine>. *Acta Crystallogr. D Biol. Crystallogr.* **2012**, *68* (4), 352–367.

(75) Emsley, P.; Lohkamp, B.; Scott, W. G.; Cowtan, K. Features and Development of *Coot*. *Acta Crystallogr. D Biol. Crystallogr.* **2010**, *66* (4), 486–501.

(76) Karplus, P. A.; Diederichs, K. Linking Crystallographic Model and Data Quality. *Science* **2012**, *336* (6084), 1030–1033.

(77) Afonine, P. V.; Moriarty, N. W.; Mustyakimov, M.; Sobolev, O. V.; Terwilliger, T. C.; Turk, D.; Urzhumtsev, A.; Adams, P. D. FEM: Feature-Enhanced Map. *Acta Crystallogr. D Biol. Crystallogr.* **2015**, *71* (3), 646–666.

(78) Moriarty, N. W.; Grosse-Kunstleve, R. W.; Adams, P. D. Electronic Ligand Builder and Optimization Workbench (eLBOW): A Tool for Ligand Coordinate and Restraint Generation. *Acta Crystallogr. D Biol. Crystallogr.* **2009**, *65* (10), 1074–1080.

(79) Chen, V. B.; Arendall, W. B.; Headd, J. J.; Keedy, D. A.; Immormino, R. M.; Kapral, G. J.; Murray, L. W.; Richardson, J. S.; Richardson, D. C. MolProbity : All-Atom Structure Validation for Macromolecular Crystallography. *Acta Crystallogr. D Biol. Crystallogr.* **2010**, *66* (1), 12–21.

(80) *The PyMol Molecular Graphics System, Version 1.7.4, Schrodinger, LLC.*

(81) Holst, M. Adaptive Numerical Treatment of Elliptic Systems on Manifolds. *Adv. Comput. Math.* **2001**, *15* (1–4), 139–191.

(82) Baker, N. A.; Sept, D.; Joseph, S.; Holst, M. J.; McCammon, J. A. Electrostatics of Nanosystems: Application to Microtubules and the Ribosome. *Proc. Natl. Acad. Sci.* **2001**, *98* (18), 10037–10041.

(83) Dolinsky, T. J.; Nielsen, J. E.; McCammon, J. A.; Baker, N. A. PDB2PQR: An Automated Pipeline for the Setup of Poisson–Boltzmann Electrostatics Calculations. *Nucleic Acids Res.* **2004**, *32* (suppl 2), W665–W667.

(84) Dolinsky, T. J.; Czodrowski, P.; Li, H.; Nielsen, J. E.; Jensen, J. H.; Klebe, G.; Baker, N. A. PDB2PQR: Expanding and Upgrading Automated Preparation of Biomolecular Structures for Molecular Simulations. *Nucleic Acids Res.* **2007**, *35* (suppl 2), W522–W525.

(85) Racker, E. Spectrophotometric Measurement of Hexokinase and Phosphohexokinase Activity. *J. Biol. Chem.* **1947**, *167* (3), 843–854.

(86) Leatherbarrow, R. J. *GraFit Version 7*; Erithacus Software Ltd: Horley, U.K., 2009.

(87) Goliĉnik, M.; Stojan, J. Slow-Binding Inhibition: A Theoretical and Practical Course for Students. *Biochem. Mol. Biol. Educ.* **2004**, *32* (4), 228–235.

Table of Contents graphic